Flow aware parameterizations invigorate the simulated ocean circulation under the Pine Island ice shelf, West Antarctica

Timothy A Smith[1,1]

[1]Cooperative Institute for Research in Environmental Sciences at the University of Colorado Boulder

November 30, 2022

Abstract

Warm, subsurface ocean waters that access ice shelves in the Amundsen Sea are likely to be a key driver of high meltrates and ice shelf thinning. Numerical models of the ocean circulation have been essential for gaining understanding of the mechanisms responsible for heat delivery and meltrate response, but a number of challenges remain for simulations that incorporate this region. Here, we develop a suite of numerical experiments to explore how sub ice shelf cavity circulation and meltrate patterns are impacted by parameterization schemes for (1) subgrid-scale ocean turbulence, and (2) ice-ocean interactions. To provide a realistic context, our experiments are developed to simulate the ocean circulation underneath the Pine Island ice shelf, and validated against mooring observations and satellite derived meltrate estimates. Each experiment is forced with data-informed open boundary conditions that bear the imprint of the gyre in Pine Island Bay. We find that even at a ˜600 m grid resolution, flow aware ocean parameterizations for subgrid-scale momentum and tracer transfer are crucial for representing the circulation and meltrate pattern accurately. Our simulations show that enhanced meltwater diffusion near the ice-ocean interface intensifies near wall velocities via thermal wind, which subsequently increases meltrates near the grounding line. Incorporating a velocity dependent ice-ocean transfer coefficient together with a flow aware ocean turbulence parameterization therefore seems to be necessary for modelling the ocean circulation underneath ice shelves in the Amundsen Sea at this resolution.

Flow aware parameterizations invigorate the simulated ocean circulation under the Pine Island ice shelf, West Antarctica

Timothy A. Smith[1,2,3]

[1]Oden Institute for Computational Engineering and Sciences, The University of Texas at Austin, Austin, Texas
[2]Cooperative Institute for Research in Environmental Sciences (CIRES) at the University of Colorado Boulder
[3]National Oceanic and Atmospheric Administration (NOAA) Physical Sciences Laboratory (PSL)

Key Points:

- Modelled meltrate and hydrography best represent observations when both ice-ocean and ocean turbulence parameterizations are flow aware
- Ocean eddy parameterizations that link momentum and buoyancy closures capture enhanced cavity flow generated by meltwater fluxes
- The invigorated circulation manifests as cyclonic gyres, bounded by an ice plain and a bathymetric ridge

Corresponding author: Timothy A. Smith, `tim.smith@noaa.gov`

Abstract

Warm, subsurface ocean waters that access ice shelves in the Amundsen Sea are likely to be a key driver of high meltrates and ice shelf thinning. Numerical models of the ocean circulation have been essential for gaining understanding of the mechanisms responsible for heat delivery and meltrate response, but a number of challenges remain for simulations that incorporate this region. Here, we develop a suite of numerical experiments to explore how sub ice shelf cavity circulation and meltrate patterns are impacted by parameterization schemes for (1) subgrid-scale ocean turbulence, and (2) ice-ocean interactions. To provide a realistic context, our experiments are developed to simulate the ocean circulation underneath the Pine Island ice shelf, and validated against mooring observations and satellite derived meltrate estimates. Each experiment is forced with data-informed open boundary conditions that bear the imprint of the gyre in Pine Island Bay. We find that even at a $\sim$600 m grid resolution, flow aware ocean parameterizations for subgrid-scale momentum *and* tracer transfer are crucial for representing the circulation and meltrate pattern accurately. Our simulations show that enhanced meltwater diffusion near the ice-ocean interface intensifies near wall velocities via thermal wind, which subsequently increases meltrates near the grounding line. Incorporating a velocity dependent ice-ocean transfer coefficient together with a flow aware ocean turbulence parameterization therefore seems to be necessary for modelling the ocean circulation underneath ice shelves in the Amundsen Sea at this resolution.

Plain Language Summary

Along the Antarctic coastline, ice shelves form where grounded glaciers reach the sea and form floating extensions over the ocean surface. Ice shelves are important for climate because they hold back land ice from reaching the ocean and contributing to sea level rise. In some regions of Antarctica, warm ocean waters can access ice shelves and lead to ice shelf melting and increased glacial mass loss. Simulating the ocean waters that reach ice shelves remains challenging, however, because it is difficult to accurately represent turbulence in the ocean and interactions at the ice-ocean interface. In this study, we show results that can provide practical guidance for accurately capturing these processes in computer models. We focus on developing a simulation of the ocean circulation under the Pine Island ice shelf, which is fed by one of the fastest flowing glaciers in Antarctica. We show that when the speed of ocean currents is used to determine the rate of heat and salt exchanges due to turbulence, the resulting simulation resembles observations.

1 Introduction

Ice shelves in the Amundsen Sea in West Antarctica are characterized by high basal meltrates, and account for roughly a quarter of the meltwater flux from the Antarctic continent over the last two decades (Adusumilli et al., 2020). For many of the ice shelves in the Amundsen Sea, high meltrates lead to ice shelf thinning, which reduces lateral buttressing: a mechanism responsible for holding back upstream ice from reaching the sea (e.g. Dupont & Alley, 2005). Decreased buttressing can therefore lead to an increase in mass loss from grounded ice, and sea level rise (Gudmundsson et al., 2019; Fürst et al., 2016).

Numerical models of the ocean circulation in the Amundsen Sea have been essential for understanding the link between ocean forcing and ice shelf melting in the region. For instance, modelling efforts have repeatedly shown that relatively warm Circumpolar Deepwater (CDW) is driven onto the continental shelf by Ekman pumping at the shelf edge, (Thoma et al., 2008; Webber et al., 2018; Dotto et al., 2019). The CDW is then steered topographically via troughs to the base of the ice shelves (e.g. St-Laurent et al., 2012; Nakayama et al., 2019, 2017; Kimura et al., 2017; Nakayama et al., 2018).

However, a number of challenges remain for computational models of the Amundsen Sea. For example, the simulated ocean circulation underneath ice shelves and estimated meltrates are highly sensitive to ice shelf topography and bathymetry (Goldberg et al., 2020, 2019; De Rydt et al., 2014; Schodlok et al., 2012). Uncertain parameters in the representation of ice-ocean interactions, e.g. the drag coefficient at the ice-ocean interface, can further lead to variation in the intensity of the ocean circulation and meltwater flux (Dansereau et al., 2014). Finally, the impact of subgrid-scale ocean turbulence parameterizations on the cavity circulation and ice shelf meltrate is unclear. In this study, we primarily focus on the last of these issues.

Modelling the Amundsen Sea requires a high horizontal grid resolution. Resolving mesoscale phenomena on the Antarctic continental shelf requires a grid resolution of ∼1-2 km (Mack et al., 2019), owing to weak stratification, shallow depths, and a large Coriolis parameter at high latitudes (Dinniman et al., 2016). Explicitly resolving processes at this scale is important because mesoscale eddies play an important role in carrying CDW onto the continental shelf (Martinson & McKee, 2012; Stewart & Thompson, 2015). Resolution requirements become even stricter as one tries to represent processes inside ice shelf cavities with greater detail. Årthun et al. (2013) showed that capturing the flow of high salinity shelf water into an ice shelf cavity requires a sub-kilometer grid resolution. Here, we model the circulation underneath the Pine Island ice shelf using a ∼600 m grid resolution. Even at this resolution, however, we show that subgrid-scale parameterization choices are critical for accurately representing the cavity circulation and ice-ocean interactions.

Dansereau et al. (2014) use a suite of numerical experiments to study the impact of various parameterization choices at the ice-ocean boundary on meltwater flux representation and the sub ice shelf circulation. They show that using an ice-ocean transfer parameterization that is dependent on the near-wall velocity is physically justifiable as it captures high meltrates at the location of strong outflow plumes and fast mixed layer currents. However, their simulations exhibit low meltrates near the grounding line, which contradicts recent observational estimates that show some of the highest meltrates exist in this grounding zone (e.g. Shean et al., 2019).

Here, we resolve this apparent conundrum by studying ice-ocean boundary parameterizations *in conjunction with* subgrid-scale parameterizations for the transfer of momentum and tracer properties. To this aim, we focus on simulating the ocean circulation underneath the Pine Island ice shelf, building on models developed by Heimbach and Losch (2012) and Dansereau et al. (2014). We use a recent estimate of Antarctic bedrock and ice shelf topography (Morlighem et al., 2020; Morlighem, 2019) and data-informed open boundary conditions to prescribe the flow into and out of Pine Island Bay. With this setup, we develop a suite of numerical experiments that test a variety of parameterization schemes for the representation of subgrid-scale ocean turbulence and fluxes at the ice-ocean interface. To validate our experiments, we compare to in situ ocean observations taken during the austral summers of 2009 and 2014 (Christianson et al., 2016; S. S. Jacobs et al., 2011), and satellite-derived meltrate fields (Shean et al., 2019). Finally, we discuss the physical mechanisms which link the representation of subgrid-scale ocean turbulence to simulated meltrates via the resolved cavity circulation. We note that while our experiments are based on a realistic representation of the cavity circulation underneath the Pine Island ice shelf, we expect that the mechanisms discussed here would generalize to other ice shelves in the Amundsen Sea.

2 Methods

2.1 Study area and model setup

Our goal in this study is to provide understanding for the various parameterization choices available to ocean-only models that simulate the circulation under ice shelves in the Amundsen Sea. As such, we develop a number of numerical experiments to test how these parameterizations impact the cavity circulation under the Pine Island ice shelf. The unique configuration for each experiment is shown in Table 1. Here we outline the study region and general model configuration that is applicable to all experiments.

The computational domain includes the cavity underneath the Pine Island ice shelf. It extends westward to 102.75°W, and northward to approximately 74.46°S, see Figure 1. Temperature, salinity, and zonal velocity is specified at the western open boundary, and these are derived from observations - see section 3.1 (more details are available in the supporting information). The western boundary is chosen to be approximately at the center of the gyre in Pine Island Bay (A. M. Thurnherr et al., 2014), such that at the open boundary specifying zonal velocities, which is the component normal to the boundary, is sufficient. The northern boundary is assumed to be closed because only 2% of the area is open.

We use the Massachusetts Institute of Technology general circulation model (MITgcm) (Campin et al., 2021; Marshall et al., 1997) to simulate the fluid flow underneath the ice shelf, approximating the flow as Boussinesq, hydrostatic, and incompressible. We omit the representation of sea ice because observations show that Pine Island Bay is largely free of sea ice during the simulated time period (Scambos et al., 1996), see section 2.4. We specify the bathymetry and ice topography by regridding output from BedMachine Antarctica v1 (Morlighem, 2019; Morlighem et al., 2020) onto a spherical polar grid using the conservative regridding alorithm from Zhuang et al. (2020). Our nominal horizontal grid spacing is 600 m $\times$ 600 m. We discretize the vertical coordinate into 62 vertical levels that are 20 m tall. The resolution of our model is chosen to balance computational efficiency while capturing the sub-kilometer scale channels in the ice, (e.g. Dutrieux et al., 2013), which are evident in the BedMachine dataset. The vertical grid uses a partial cell approach to approximate partially closed grid cells at the intersection with ice topography or bathymetry (Adcroft et al., 1997), where the minimum cell size is 2 m.

We remove ice from grid cells where the regridded ice topography is only < 0.2 m, such that these grid cells are ice-free. We remove ice from these areas because the computed heat fluxes in these areas is unreasonably high, due to a division by the ice thickness. We note that the cutoff chosen here (0.2 m) is arbitrary, and we found values less than ~ 5 m to have little impact on the equilibrium state of the model. The ice shelf is assumed to be floating in isostatic equilibrium on top of the water column. We use the Jackett and McDougall (1995) formulation for the equation of state. All simulations use a virtual salt flux and a linear free surface formulation. With a virtual salt flux, meltwater does not add volume locally to the water column and we therefore found the nonlinear free surface (Campin et al., 2004) to have a negligible impact on the model's equilibrium state.

We approximate an initial condition for the model spinup by "extruding" the temperature and salinity open boundary conditions in the longitudinal direction to cover the whole domain, and use an initial velocity field of 0 m/s. All models are then integrated forward in time for ten years with a quasi-second order Adams-Bashforth method, at which point an approximate steady state is reached. All model quantities shown are computed as an average over the final year of spinup. All experiments use a time step of 150 s for numerical stability, except for `Leith` and `QGLeith` (section 2.3), which are able to use a larger time step without diminishing the representation of the ocean state (Fox-Kemper & Menemenlis, 2008), see Table 1.

Table 1. Configuration summary for each numerical experiment performed. Each experiment takes on the parameter values or description given for the `base` experiment, unless noted otherwise. See section 2.3 for the definitions of ν_L and ν_{4L}.

Experiment Name	Ice-Ocean Thermal Transfer Coefficient	Viscosity	Diffusivity	Δt
`base`	$\gamma_T = f(u^*)$	Flow Independent $\nu_h = 0.2\,\nu_L$ $\nu_{4h} = 0.02\,\nu_{4L}$ $\nu_r = 10^{-4}$ m^2/s	Flow Independent $\kappa_h = 0.01$ m^2/s $\kappa_r = 10^{-4}$ m^2/s	150 s
`constIO`	$\gamma_T = 10^{-4}$			
`smallVisc`		$\nu_h = 0.03\,\nu_L$ $\nu_{4h} = 0.003\,\nu_{4L}$		
`Leith`		Flow Aware $C_{\text{Leith}} = 2$ $C_{\text{4Leith}} = 2$		300 s
`QGLeith`		Flow Aware $C_{\text{QGLeith}} = 2$	Flow Aware $C_{\text{QGLeith}} = 2$	300 s

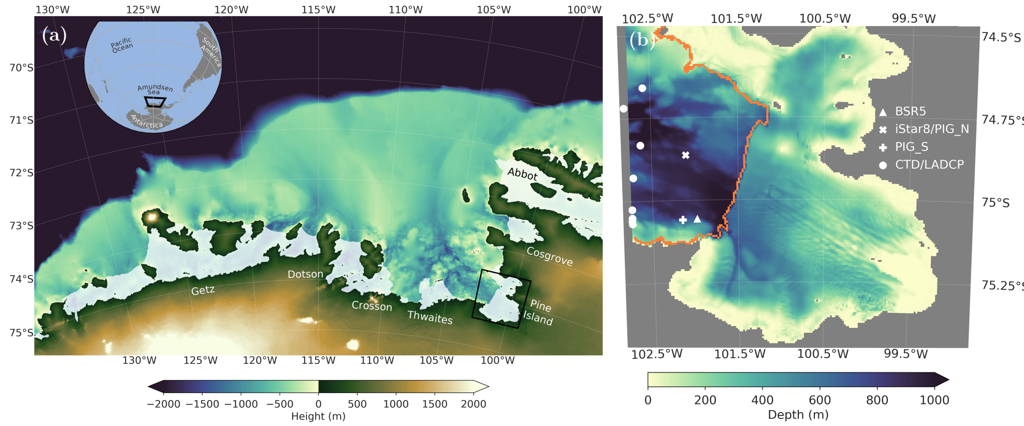

Figure 1. The study area. (a) The Amundsen Sea, West Antarctica. The region's location relative to Antarctica is indicated by the box in the globe in the upper left corner. The colorbar indicates bathymetry on the continental shelf and height of land ice. The white areas refer to the major floating ice shelves in the region, and the computational domain is indicated by the box around the Pine Island ice shelf. The topography and ice shelf locations are from BedMachine Antarctica (Morlighem et al., 2020; Morlighem, 2019). (b) Water column depth of the computational domain. Depth is obtained after regridding the ice topography and bathymetry shown in panel (a). The orange line shows the approximate icefront location, such that the Pine Island ice shelf lies to the east. Locations of observations used in this study are shown in white.

2.2 Parameterizations at the ice-ocean boundary

We represent the exchanges of heat and salt fluxes at the ice-ocean boundary with the three equation model (Hellmer & Olbers, 1989), in its conservative formulation following Jenkins et al. (2001). This parameterization amounts to a balance of heat and salt fluxes at the ice-ocean interface, along with a linearized equation of state:

$$
\begin{aligned}
-qS_b &= Q_m^S \\
-L_m q &= Q_m^T + Q_I^T \\
T_b &= aS_b + b\phi_b + c\,.
\end{aligned}
$$

Here $L_m = 334$ kJ/kg is the latent heat of melting, a, b, c are empirical constants, q is the meltrate as a mass flux where negative (positive) values imply melting (freezing), and T_b, S_b, and ϕ_b are the in situ temperature, salinity, and pressure at the base of the ice shelf which are assumed to be at the freezing point. The term Q_I^T is a diffusive flux of heat through the ice (Holland & Jenkins, 1999), and Q_m^T, Q_m^S are the fluxes of heat and salt through a boundary layer in the ocean just below the ice shelf:

$$
\begin{aligned}
Q_m^T &= \rho_0 \gamma_T (T - T_b) \\
Q_m^S &= \rho_0 \gamma_S (S - S_b)\,,
\end{aligned}
$$

where $\rho_0 = 1030$ kg/m^3 is the reference density and T, S are the in situ temperature and salinity in the boundary layer just below the ice shelf. The most important parameter choice in the three equation model is the specification of the heat and salt transfer coefficients, γ_T and γ_S (Holland & Jenkins, 1999), which represent the rate of heat and salt transfer through the oceanic boundary layer.

As a simplified case, in the `constIO` experiment we use a simple constant to specify the thermal transfer coefficient $\gamma_T = 10^{-4}$, Table 1. For this constant coefficient case, we make the assumption that $\gamma_S = 5.05 \times 10^{-3} \gamma_T$. In all other experiments, we use a form of the transfer coefficients that is dependent on the near wall velocity:

$$\gamma_{T,S} = \Gamma_{T,S} u^* ,$$

where $\Gamma_{T,S}$ are turbulent exchange coefficients (see Holland and Jenkins (1999) and Appendix B in Dansereau et al. (2014) for details). The friction velocity is:

$$u^* = \sqrt{C_d U_M^2} ,$$

where $C_d = 1.5{\times}10^{-3}$ is the drag coefficient at the ice-ocean interface, and U_M is the near wall velocity:

$$(U_M)_{i,j} = \sqrt{\frac{1}{2}\left[(\bar{u}_i^{BL})^2 + (\bar{u}_{i+1}^{BL})^2\right] + \frac{1}{2}\left[(\bar{v}_j^{BL})^2 + (\bar{v}_{j+1}^{BL})^2\right]} .$$

Here $\bar{(\cdot)}^{BL}$ denotes a vertical volumetric average over a boundary layer that is one grid cell (20 m) thick, and i and j denote zonal and meridional grid cell indices, respectively. This formulation takes into account the boundary layer parameterization outlined in Losch (2008), such that the volume underneath the ice shelf that is used to compute vertical fluxes is constant, no matter where the vertical grid intersects with the ice shelf topography. Horizontal averaging is necessary because of the Arakawa C grid discretization (Arakawa & Lamb, 1977).

2.3 Parameterizations of subgrid ocean turbulence

Representing the effect of subgrid-scale ocean turbulence on the transport of momentum, heat, and salt is a crucial aspect of any ocean model. Here we make the common assumption that these effects can be captured with a dissipative Laplacian and/or biharmonic operator. In the following discussion we explain how the horizontal viscosity and diffusivity, ν_h and κ_h, respectively, are defined for each experiment. We add a background vertical viscosity and diffusivity of $\nu_r = 10^{-4}$ m^2/s and $\kappa_r = 10^{-4}$ m^2/s, respectively, in all experiments.

It is often the case that viscosity and diffusivity coefficients are chosen to be constant, or to vary weakly with the grid scale of the domain (e.g. Mack et al., 2019; Dansereau et al., 2014; Heimbach & Losch, 2012; Goldberg et al., 2019, 2020). We consider this to be our starting point, and use viscosity and diffusivity coefficients that are approximately constant for the `base`, `constIO`, and `smallVisc` experiments, see Table 1. In these experiments the Laplacian and biharmonic viscosities are chosen to be a fraction of:

$$\nu_L = \frac{L^2}{4\Delta t} \qquad \nu_{4L} = \frac{L^4}{32\Delta t}$$

based on the CFL criterion for numerical stability (Griffies & Hallberg, 2000), where L is the local grid scale:

$$L = \sqrt{\frac{2}{(\Delta x)^{-2} + (\Delta y)^{-2}}} . \tag{1}$$

With a nominal grid spacing such that $L \simeq 600$ m across the domain, and $\Delta t = 150$ s for these four experiments, the Laplacian (biharmonic) viscosity is roughly 120 m^2/s (540,000 m$^4/s$) for `base` and `constIO`, and 18 m^2/s (81,000 m^4/s) for `smallVisc`. We note that the viscosity values for the first two experiments appear to be high, but are necessary for numerical stability in `constIO`. We therefore use the same values in `base` for comparison. We specify only a Laplacian diffusivity for horizontal tracer transport, which is taken as a small constant following the "do no harm" principle, (e.g. Fox-Kemper & Menemenlis, 2008). The idea behind this principle is to avoid damping the effect of eddy induced tracer transport that is already resolved.

Previous studies of eddy activity on the marine margins of Antarctica have shown that these regions exhibit a wide range of spatial scales relevant to the transfer of momentum, heat, and salt (Mack et al., 2019; Årthun et al., 2013; Hattermann et al., 2014). Figure 2 (a) shows that even in this relatively small regional domain, the cavity-type geometry of the ice shelf and highly variable bathymetry impose a range of scales to be represented. Specifically, Figure 2 (a) displays the ratio of the local grid scale (equation (1)) to the first baroclinic Rossby radius of deformation given by Chelton et al. (1998):

$$L_D = \frac{1}{\pi|f|}\int_{-H}^{0}\sqrt{-\frac{g}{\rho_0}\frac{\partial\rho}{\partial z}}\,dz\,. \tag{2}$$

Near the grounding line this ratio is below 2, such that the effect of the largest eddies and baroclinic instabilities are only partially resolved (Hallberg, 2013). On the other hand, farther away from the grounding line the resolution is well above the deformation radius. Therefore, even at this sub-kilometer resolution, the model is in a gray zone, motivating us to test parameterizations that are "flow aware". Flow aware parameterizations adjust their local impact based on properties of the resolved flow (Bachman et al., 2017). In the following paragraphs, we describe the flow aware parameterizations used in our numerical experiments.

First, we test the flow aware parameterization developed by C. E. Leith (1968); C. Leith (1996), with the biharmonic stabilization suggested by Fox-Kemper and Menemenlis (2008). The Leith parameterization is motivated by representing the enstrophy cascade present in 2D turbulence. The specification of nondimensional parameters for the experiments `Leith` (Table 1) are chosen for numerical stability. In these simulations, it is unclear how to specify the diffusivity field, and we therefore tested the effect of various formulations for the diffusivity tensor and intensity κ_h. With a diffusivity tensor acting aligned with the grid, we tested $\kappa_h = 1.0$ m^2/s, which made no discernible difference to $\kappa_h = 0.1$ m^2/s in `Leith`. We additionally tested the effect of rotating the diffusion tensor along isopycnals as in Redi (1982), and found that this had a negligible effect on the resulting simulation as well.

Our final experiment uses a recently developed parameterization termed QG Leith (Bachman et al., 2017). We find this scheme to be advantageous from a modelling perspective because it provides theoretical grounding for the specification of unresolved, eddy-induced effects in the tracer equations as well as in the momentum equation. Specifically, the scheme results in a formulation of an eddy viscosity, ν_h, and suggests to set the transfer coefficient of the Gent and McWilliams (1990) (GM) eddy advection transfer coefficient such that $\kappa_{GM} = \nu_h$. In our simulations we use the skew flux implementation of the GM scheme (Griffies, 1998), such that $\kappa_\rho = \kappa_{GM} = \nu_h$. The resulting diffusion tensor is:

$$\kappa_\rho \begin{pmatrix} 1 & 0 & 0 \\ 0 & 1 & 0 \\ 2S_x & 2S_y & |S|^2 \end{pmatrix},$$

where $S_x = -\partial_x\sigma/\partial_z\sigma$ and $S_y = -\partial_y\sigma/\partial_z\sigma$ are the isoneutral slopes and σ is the locally referenced potential density. While this formulation implies a small vertical diffusivity, we add an additional background value of $\kappa_r = 10^{-4}$ m^2/s for numerical stability.

The time-averaged Laplacian viscosities obtained from the final year of a ten year spinup are shown in Figure 2 (b & c) for `Leith` and `QGLeith`, respectively. The viscosity fields show that the impact of a flow aware subgrid parameterization is particularly important. In both experiments viscosities are as high as ∼60 m^2/s in a large southern channel (marked by a black triangle in Figure 2(b)) and along the icefront, where there is strong shear due to interaction with the ice shelf topography. The biggest differences between the two viscosity fields are seen near the black dot in Figure 2(b), where the water column is <50 m deep. The larger values in `QGLeith` are due to a physcial mecha-

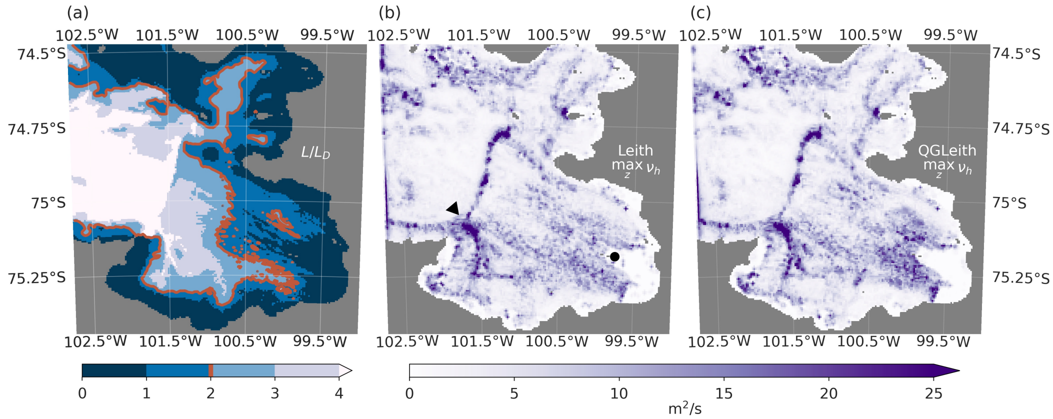

Figure 2. (a) The ratio of the grid scale to the first baroclinic Rossby radius of deformation L/L_D, see equations (1) & (2). A red contour line is added to emphasize where the grid scale is approximately twice the deformation radius. (b & c) Nonlinear Laplacian viscosities computed in the `Leith` (b) and `QGLeith` (c) experiments. The maximum value over the vertical dimension is shown as a representative view. The high spatial variability results from the fact that the Leith and QG Leith parameterizations are flow aware. All other experiments use a viscosity coefficient that is nearly constant across the domain. The black triangle in panel (b) marks the location of a southern channel in the ice shelf topography, and the black circle approximately marks the furthest seaward extent of an ice plain (discussed in section 3.3).

nism discussed in section 3.3, which arises because the QG Leith parameterization specifies flow aware diffusivities as well as viscosities.

Finally, we note that we also tested the effect of using the parameterization presented in Griffies and Hallberg (2000); Smagorinsky (1963). In our experiments, this scheme produced similar viscosity values as shown for `Leith` and had negligible differences on the results, so we omit its presentation.

2.4 In situ ocean observations

In this study we use observations of the ocean hydrography in Pine Island Bay taken from moorings, Conductivity, Temperature, and Depth (CTD) casts, and velocity from Lowered Acoustic Doppler Current Profiler (LADCP) casts (Christianson et al., 2016; S. S. Jacobs et al., 2011; Dutrieux et al., 2014; Assmann et al., 2013; Webber et al., 2017). Figure 1 shows the location of the moorings used: BSR5, iStar8, PIG_N, and PIG_S. The moorings provide a long temporal record at fixed locations, and approximately cover the time periods: 2009-2014 (BSR5) (S. Jacobs & Huber, 2015; Carbotte et al., 2007), 2012-2014 (iStar8), and 2014-2016 (PIG_S & PIG_N). The CTD and LADCP casts (A. Thurnherr, 2015; Carbotte et al., 2007) provide a snapshot of the ocean state at many locations throughout Pine Island Bay and, due to weather constraints, can only be taken during austral summer.

Here we use the data for two purposes. First, we use CTD and LADCP data near the open boundary of the domain (white dots in Figure 1) to generate data-informed open boundary conditions via optimal interpolation. Specifically, we use CTD and LADCP casts taken during 2009 and 2014 (A. Thurnherr, 2015). We find that it is appropriate to blend the data taken separately during 2009 and 2014 because the mean state (e.g. thermocline depth) is roughly similar in Pine Island Bay during these years (Webber et al., 2017). Details on how we use these data to obtain open boundary conditions for the model are described in the supporting information.

Secondly, we use the mooring data within the computational domain to validate (or invalidate) the equilibrium state of the numerical experiments described previously. For this task, we must choose a subset of the mooring data that is consistent with the data that is used to obtain the open boundary conditions. Therefore, we select data taken from January through March during 2009 and 2014 as available from each of the moorings. We note that it would be inconsistent to use data from 2011-2013 for this task, as there was a documented cooling in Pine Island Bay (Webber et al., 2017). Finally, Pine Island Bay is largely free of sea ice during January through March from 2009-2014 (Scambos et al., 1996). This is consistent with our modelling assumption that sea ice is excluded.

We compute the temporal mean and standard deviation of the mooring data at each instrument location during the time periods outlined above to obtain a representative state we can compare our models to. At most depth levels the temporal standard deviation, σ, is small, so we prescribe the minimum values:

$$\begin{aligned}\sigma_{M,\theta} &= \max(0.25, \sigma)\,^{\circ}\mathrm{C}\\ \sigma_{M,S} &= \max(0.025, \sigma)\,\mathrm{g/kg}\,,\end{aligned}$$

which provides a means of representation error, i.e. error due to misrepresentation of point data within the model grid cells. Using these minimum values also accounts for potential conflicts between different observed values that correspond to the same grid cell, or nearby neighbors. More details related to raw mooring data processing, including considerations involved with computing potential temperature from in situ temperature, are provided in Appendix A.

3 Results

3.1 Data-informed open boundary conditions

The open boundary conditions resulting from optimally interpolating the 2009 and 2014 CTD and LADCP data are shown in Figure 3. The upper row shows the potential temperature (a), salinity (b), and zonal velocity (c). We highlight a few noteworthy features in the open boundary conditions. The zonal velocity (Figure 3(c)) clearly shows the gyre-structure noted in previous work (A. M. Thurnherr et al., 2014), which approximates the center of the gyre to be at approximately 74.875°S. For reference, we compute the location of zero velocity to be at about 74.871°S, for depths above 300 m. The strongest flows are $\sim 0.1-0.22$ m/s in magnitude, and preside at depths shallower than 400 m. The hydrography shows relatively warm (> 1°C) and salty (> 34.65 g/kg) waters below 600 m depth that is likely CDW fed. This vertical structure is consistent with previous studies (e.g. Christianson et al., 2016; Nakayama et al., 2019). At the center of the gyre there is a notable rise in the thermocline (Figure 3(a)) and halocline (Figure 3(b)). At the southern and northern boundaries of the gyre, the 0°C isotherm lies at (75.1°S, 375 m) and (74.64°S, 350 m), respectively, and elevates to its shallowest depth at approximately (74.875°S, 200 m). The elevated thermocline and halocline could be driven by upwelling from Ekman pumping within the gyre.

The lower row (Figure 3 (d-i)) shows the observed values compared to the optimal interpolation result for the latitudes 75.03°S and 73.66°S to highlight the inflow and outflow properties. The interpolated temperature (d & e) and salinity (f & g) fit the data well within one standard deviation. The zonal velocity (h & i) shows a weaker circulation than the observations above 300 m, but the general structure of the inflow and outflow is represented. In general, the interpolated temperature and salinity fields tend to fit the data better than the zonal velocity. We attribute the better fit to the fact that the temperature and salinity observations have a much more coherent, meridionally correlated structure. In contrast, the velocity observations show less coherence in both the

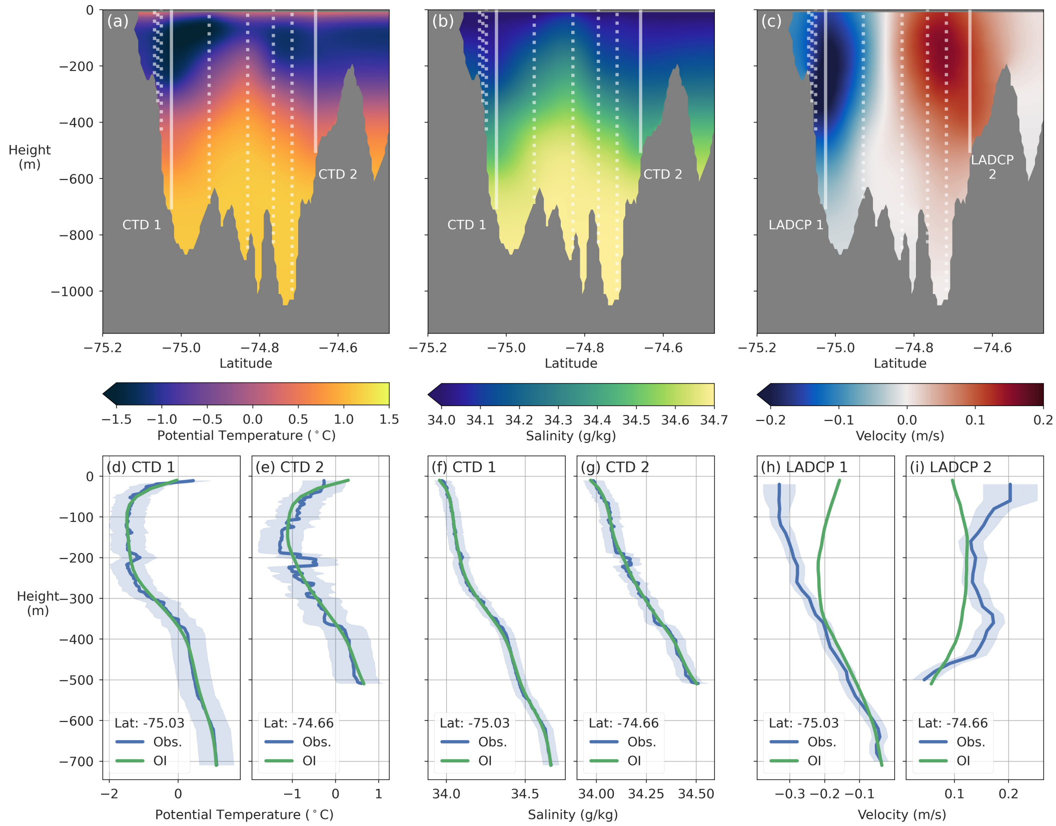

Figure 3. Data-Informed Western Open Boundary Conditions. (a-c) Fields resulting from optimally interpolating the CTD and LADCP data shown in Figure 1. Data locations are shown as faint white dotted and solid lines. (d-i) Comparison of the optimal interpolation results (OI; green line) and observational mean plus standard deviation (Obs; blue line). Each line plot corresponds to one of the two solid lines in the panel above. The selected latitudes are chosen to show the inflow and outflow of the gyre, and give a representative view of misfits. Comparisons at all observation locations are shown in the supporting information.

vertical and meridional directions. Optimal interpolation relies on filling the data gaps with a simple correlation length prescription that must be large enough to fill the space between data locations. At the same time, longer correlation length scales effectively smooth out local heterogeneities in the velocity data. The results shown here are based on numerous attempts to balance these two competing aspects of optimal interpolation. Comparisons at all CTD and LADCP data locations are shown in the supporting information.

3.2 Model comparison to mooring data

Here we compare the temperature and salinity structure computed from each numerical experiment to the Pine Island Bay mooring data. The ocean states presented here are obtained by integrating each experiment described in Table 1 forward for 10 years, subject to the boundary conditions described in section 3.1. In all cases, the values shown are an average over the final simulation year.

A summary plot of the model-data comparison is shown in Figure 4. The left two plots show a representative vertical profile of temperature (a) and salinity (b) for each

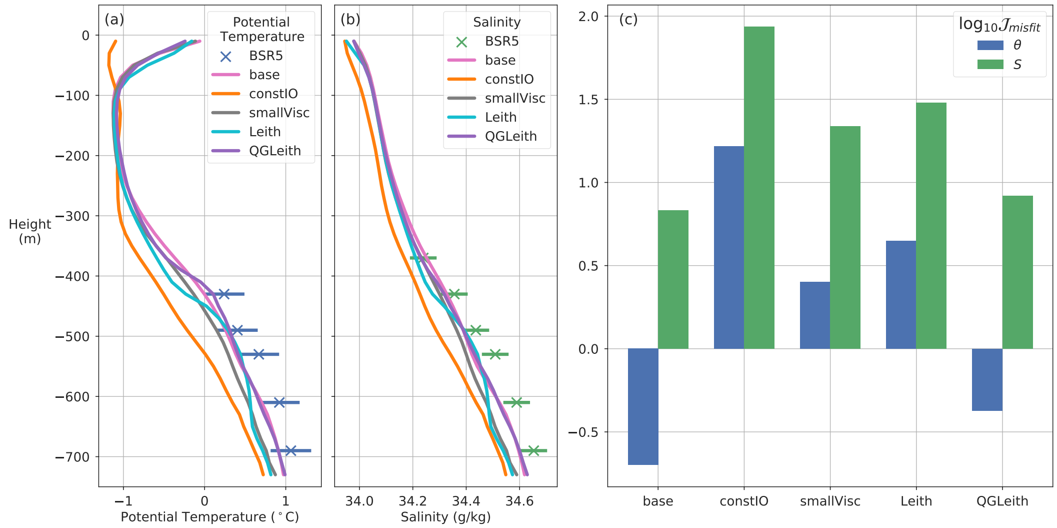

Figure 4. Comparison of the numerical experiments to mooring observations. (a-b) Profiles of potential temperature (a) and salinity (b) for each experiment (colored lines) corresponding to the BSR5 mooring data, with observed mean and standard deviation represented by the x's and horizontal bars. (c) Summary of the total misfit for each model experiment represented as $\log_{10} \mathcal{J}_{\text{misfit}}$, see equation (3). The misfit is shown separately for potential temperature (blue) and salinity (green). Lower numbers imply a better fit, and the base-10 logarithm is shown to emphasize that experiments with a value less than zero imply that the data misfit is lower than the standard deviation.

model (colored lines), compared to the mooring data (x's), or CTD data in the case of some salinity depth levels (see Appendix A). Figure 4(c) shows a quantitative comparison for each model against all of the data based on the metric $\mathcal{J}_{\text{misfit}}$:

$$\mathcal{J}_{\text{misfit}} = \left\| \frac{\mathbf{m} - \mathbf{d}}{\boldsymbol{\sigma}} \right\|_2^2 = \sum_{i}^{N_{\text{Obs}}} \left(\frac{m_i - d_i}{\sigma_i} \right)^2 . \tag{3}$$

Here $\mathbf{m} = \{m_i\}_{i=1}^{N_{\text{Obs}}}$ and $\mathbf{d} = \{d_i\}_{i=1}^{N_{\text{Obs}}}$ are the values from the model and observations at each location, i, respectively. The vector $\boldsymbol{\sigma} = \{\sigma_i\}_{i=1}^{N_{\text{Obs}}}$ consists of the standard deviations associated with each data value (section 2.4). Lower values of $\mathcal{J}_{\text{misfit}}$ imply a closer fit to the data, and we note that Figure 4(c) shows $\log_{10} \mathcal{J}_{\text{misfit}}$ such that values below zero imply that the misfit is smaller than the assumed standard deviation.

The `base` and `QGLeith` experiments produce the least error compared to the observations, fitting the data within 2 standard deviations. On the other hand, the `constIO` experiment shows the largest deviations from the data, beyond 2-3 standard deviations in many instances. In these experiments, models that use a velocity dependent ice-ocean transfer parameterization tend to fit the data better than `constIO`. This indicates that a flow aware ice-ocean parameterization is important for correctly representing the ocean circulation, even away from the ice shelf.

3.3 Evaluation of meltrate patterns

In Figure 5 we qualitatively compare the meltrate patterns generated by each model (a-e) to the 2008-2015 average value inferred from high resolution satellite-derived digital elevation models (f) (Shean et al., 2019). To enable comparison, we convert the modelled meltrates from kg/s to m/yr or Gt/yr assuming a meltwater density of 1000 kg/m^3 and 360 days per year. The meltrate is largely determined by the sub ice shelf circulation, especially since most simulations employ a velocity dependent ice-ocean transfer parameterization. We therefore present the barotropic streamfunction underneath the ice shelf to give a summarized view of the circulation in each case, Figure 6.

We note at the outset of this discussion that no model represents the broad pattern of intense melting (> 100 m/yr) just seaward of the grounding line (near the white dot in Figure 5(a) and in the hatched area of Figure 5(f)), which is a key feature in the satellite-based estimate. Instead, each model shows a dark region where meltrates are nearly zero. This region is referred to as an "ice plain" (Corr et al., 2001; Thomas et al., 2004), and in our model the ice shelf here is mostly ungrounded, with a water column height of < 50 m. The weak simulated meltrates in this region can be partially attributed to the fact that only one or two vertical grid cells in the water column are active here, such that any flow induced melting is not well resolved. The discrepancy between models and observations could be further accentuated by subglacial discharge. Drainage is not captured by the models, but satellite derived digital elevation models provide some evidence that this occurs somewhat regularly near the Pine Island Glacier grounding line, and could be a reason for high meltrates (Joughin et al., 2016). In any case, we limit our discussion here to a qualitative comparison, rather than quantitative, due to this major difference, and focus on aspects of the meltrate pattern that the ocean models can reasonably capture. To aid in the visual comparison, the region where this large discrepancy occurs is hatched in panel (f) of Figure 5.

The `base` experiment exhibits the lowest domain integrated meltrate, 24.8 Gt/yr, and a muted spatial pattern throughout the domain (Figure 5(a)). In the region surrounding the ice plain there is little melting. Some of the highest meltrates are in the southern channel, marked by the white triangle in Figure 5(a). The low meltrate in this experiment coincides with a weak circulation: the barotropic streamfunction has a maximum of 0.05 Sv under the ice shelf (Figure 6(a)). We attribute the weak circulation and low meltrates to the relatively large viscosities used.

The `smallVisc` experiment shows the effect of reducing the `base` viscosities to a value that is likely to be more practical at this resolution. In particular the circulation is much stronger underneath the ice shelf: the barotropic streamfunction is almost quadrupled to 0.18 Sv (Figure 6(c)). As a result, the total meltrate is increased to 37.8 Gt/yr (Figure 5(c)). However, the spatial pattern still exhibits relatively low values near the ice plain, particularly on the northern side.

Upon first glance, the meltrate pattern shown in the `constIO` experiment appears credible because it exhibits high meltrates near the grounding line, reaching 72 m/yr (Figure 5(b)). Additionally, the high meltrates correspond to the observations such that the highest values are obtained close to the grounding line, and attenuate farther away from this area. However, we note a few subtle, but important discrepancies with the observed spatial pattern. First, the meltrate seems to be artificially high in the northern ice shelf cavity (north of approximately 74.8°S), and it is likely the case that the simple guess of $\gamma_T = 10^{-4}$ m/s is too high in this area. Secondly, the pattern in the southern channel is exactly the opposite of what is shown in the observations and in almost all other experiments. That is, the meltrate is *lowest* exactly in the channel where the most vigorous outflow is, but it is high in the region surrounding the channel. Both of these cases show that choosing a constant coefficient ice-ocean parameterization is deficient because it does not adapt to the flow field.

Before comparing the `Leith` and `QGLeith` experiments, it is useful to note the similarities and differences between the Leith and QG Leith schemes. While the viscosity formulation is somewhat similar in Leith and QG Leith (Bachman et al., 2017), the main difference between these two parameterizations lies in the representation of tracer dif-

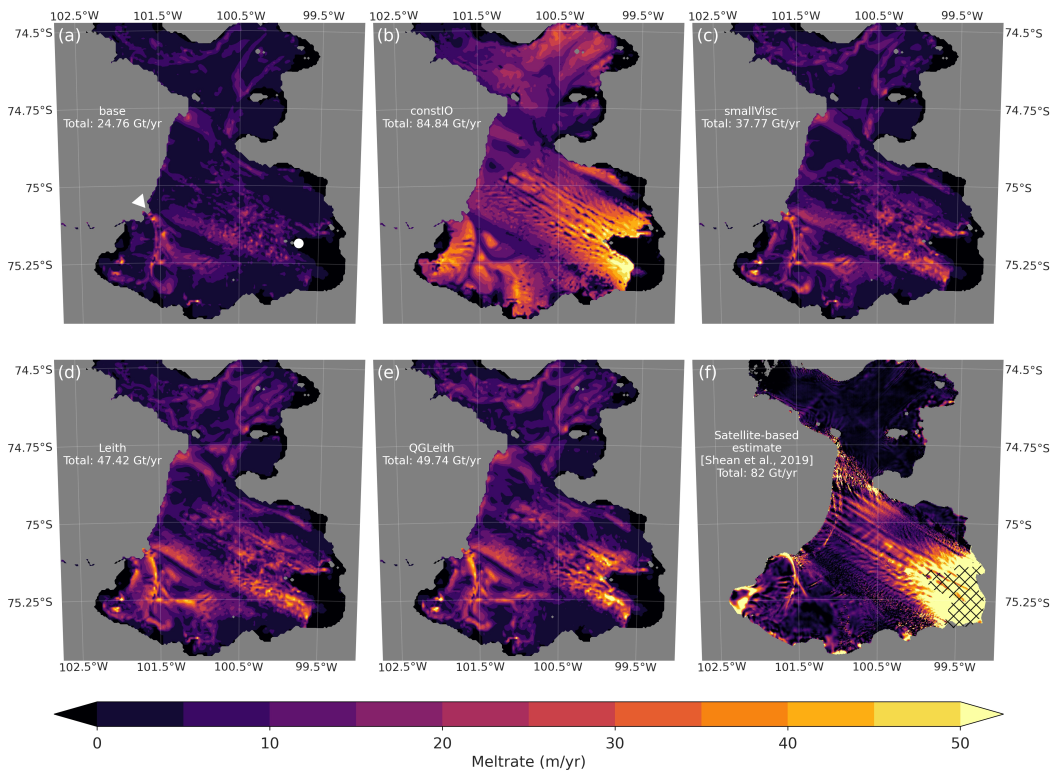

Figure 5. (a-e) Meltrate patterns computed from each numerical experiment. (f) 2008-2015 average meltrate patterns inferred from satellite observations (Shean et al., 2019). The white triangle in panel (a) marks the location of the large southern channel in the ice shelf topography, and the white circle approximately marks the furthest seaward extent of an ice plain that is discussed in the text. The hatching in panel (f) denotes the ice plain discussed in the text.

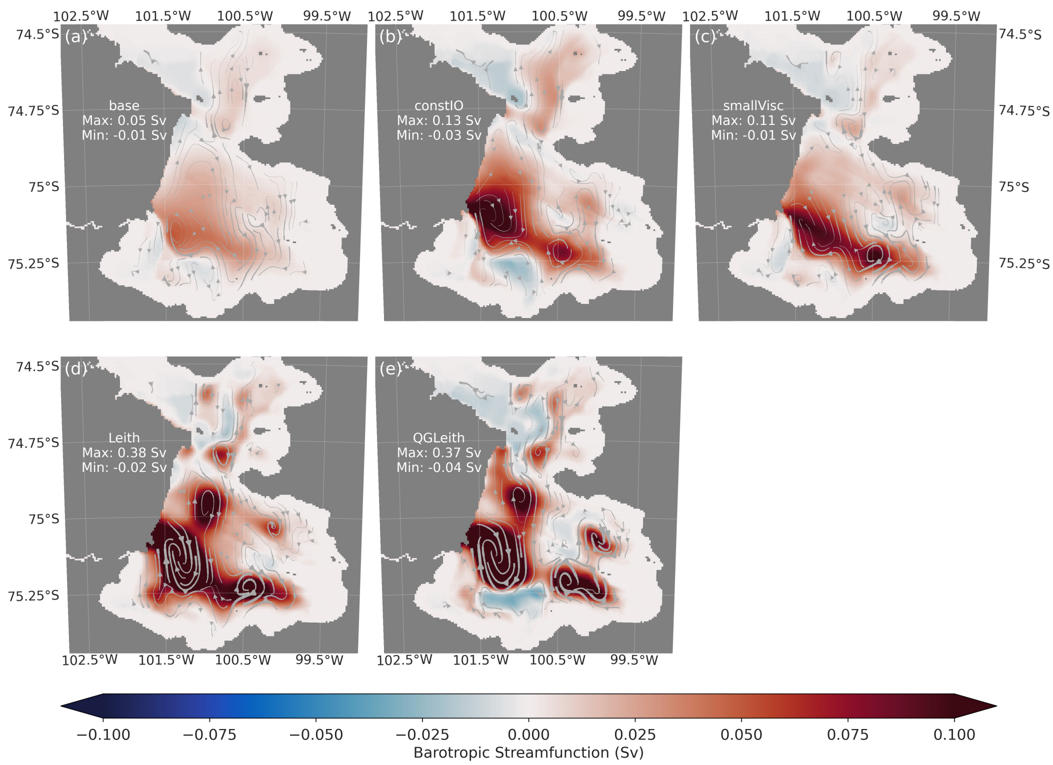

Figure 6. Barotropic streamfunction underneath the ice shelf in each experiment. Arrows indicate the sense of the circulation, and the color and linewidth indicate the intensity. The region outside of the ice shelf is omitted as all simulations show a cyclonic gyre with a maximum strength of 1.55 Sv, driven by the open boundary conditions.

fusion. Recall that when QG Leith is implemented with the skew flux implementation of GM (Griffies, 1998), the spatially varying tracer diffusion coefficient is set equal to the Laplacian viscosity values shown in Figure 2(c). The most notable difference between the `QGLeith` and `Leith` experiments is a broad pattern of high meltrate flanking the ice plain to the north and south, with values reaching up to 66 m/yr (Figure 5(e)). Correspondingly, the gyre-like flow near the grounding line is more vigorous in `QGLeith` than in `Leith`, see Figure 6(d & e). Comparing the spinup period of these two experiments explains why this accentuated meltrate pattern and enhanced flow appears in `QGLeith` but not `Leith`.

Figure 7 shows the difference between the `QGLeith` and `Leith` simulations during spinup (a-i) along a section of the domain near the grounding line indicated in panel (j). The left column (Figure 7(a,d,g)) shows the difference in the total horizontal diffusive flux of salt between the two experiments. This difference in diffusion is entirely due to the spatially varying diffusivity coefficient set by the QG Leith parameterization. Negative values indicate that the `QGLeith` experiment exhibits more diffusion of freshwater away from the ice shelf, resulting in a relatively buoyant layer surrounding the ice shelf. Note that in this domain buoyancy is largely driven by salinity differences rather than temperature differences. The middle column, Figure 7(b,e,h), shows the density difference between the two experiments, $\delta\rho = \rho_{\mathrm{QGLeith}} - \rho_{\mathrm{Leith}}$. The density difference is generally negative near the ice shelf, implying that water near the ice shelf is more buoyant in `QGLeith` than in `Leith`. This layer of buoyant water establishes a horizontal density gradient, with lighter waters close to the ice shelf and heavier waters away from the ice shelf. The horizontal density gradient subsequently enhances the flow via thermal wind balance:

$$\left(\frac{\partial u_{TW}}{\partial z}, \frac{\partial v_{TW}}{\partial z}\right) = \left(\frac{g}{f\rho_0}\frac{\partial \rho}{\partial y}, -\frac{g}{f\rho_0}\frac{\partial \rho}{\partial x}\right).$$

The right column, Figure 7(c,f,i), shows the velocity difference between the two experiments, $\delta v^{\perp} = v^{\perp}_{\mathrm{QGLeith}} - v^{\perp}_{\mathrm{Leith}}$. Here $v^{\perp}$ is the velocity normal to the section indicated in Figure 7(j). Negative (positive) values indicate that the flow toward (away from) the grounding line is larger in `QGLeith` than in `Leith`. We note that the sense of the mean flow in `Leith` and `QGLeith` is similar (Figure 6(d & e)). Therefore, the structure of the differences shown in Figure 7(c,f,i) show that the inflow and outflow is stronger in `QGLeith` than `Leith`.

The result of this mechanism is fast flowing, cyclonic "mini-gyres" on the north and south sides of the ice plain which are evident in Figure 6(e) for `QGLeith`. The flow in these gyres results in higher velocities at the ice-ocean interface, which drive larger meltrates due to the velocity-dependent formulation of the ice-ocean transfer coefficient. Considering the spatially integrated meltrate in a 15 km radius around the white circle in Figure 5(a), the invigorated flow amounts to a grounding zone meltwater flux that is 2 Gt/yr larger in `QGLeith` than `Leith`. Additionally, the maximum meltrate within this radius is about 14 m/yr larger in `QGLeith` than `Leith`, at 66 m/yr.

We note that the extent of the cyclonic gyres is, however, limited by the presence of the bathymetric ridge underneath the ice shelf. In the `QGLeith` experiment, four small cyclonic gyres are present, where the two closer to the icefront are separated from the two closer to the grounding line by the ridge. The imprint of this separation can be seen in the meltrate pattern, Figure 5(e). The enhanced meltrate due to the thermal wind driven flow stops at the bathymetric ridge, suggesting that it blocks the ocean circulation from advancing high meltrates further into the domain.

4 Discussion and outlook

In this study, we have shown that using flow aware subgrid-scale parameterizations of ocean turbulence together with a flow aware parameterization at the ice-ocean inter-

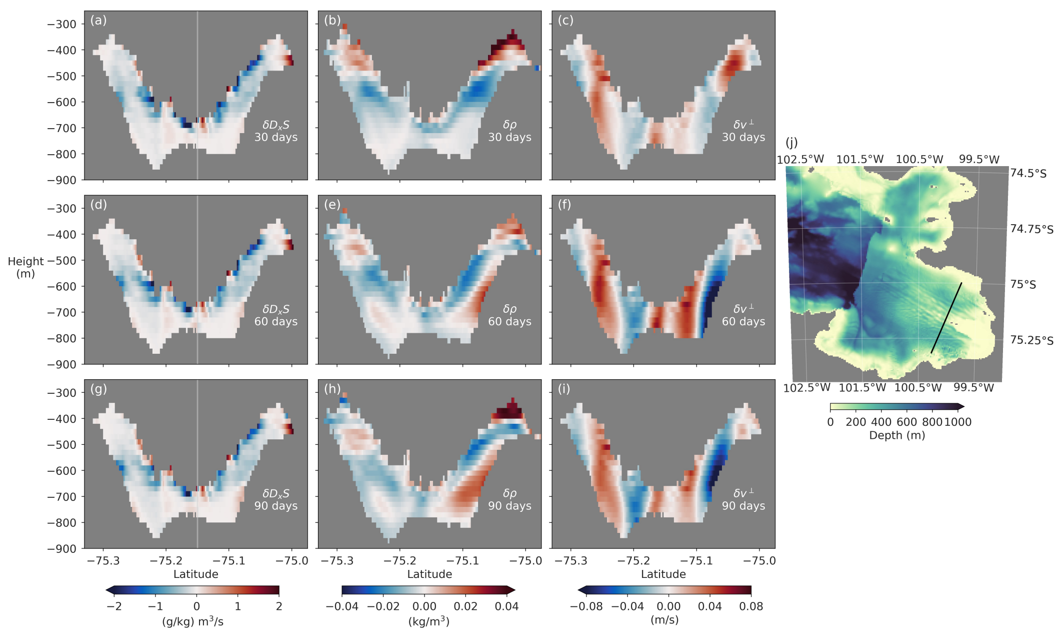

Figure 7. Comparison of `QGLeith` and `Leith` during the first 30 (a-c), 60 (d-f), and 90 (g-i) days of spinup. All quantities shown are extracted along the slice indicated by the black line in the map on panel (j). In each plot (a-i), the difference `QGLeith - Leith`, is shown, indicated by the δ. (a,d,g) The difference in the total horizontal diffusivity of salinity in the direction tangent to the black line in panel (j). Negative values indicate that there is a net transport of freshwater away from the ice shelf. We note that the field shown was modified by multiplying the values on the left side of the white line by -1 in order to aid the visualization. (b,e,h) The difference in density, where positive (negative) values indicate regions where water is heavier (lighter) in `QGLeith` than in `Leith`. (c,f,i) The difference in velocity normal to the black line in panel (j), where positive (negative) indicates stronger flow in `QGLeith` that is away from (toward) the grounding line.

face provides the most reliable means to represent the cavity circulation and meltrate pattern under the Pine Island ice shelf. Specifically, the `QGLeith` experiment shows the best balance between fitting the in situ mooring data while generating a credible meltrate pattern compared to the satellite-based estimates from Shean et al. (2019).

The results from the `base` and `constIO` experiments provide a similar conclusion to those in Dansereau et al. (2014). That is, while the velocity dependent parameterization seems to be more physically plausible in its formulation, meltrates near the grounding line are greatly diminshed compared to the constant coefficient case and observation-based estimates. Here the conundrum is further exacerbated by the fact that `constIO` deviates from the Pine Island Bay mooring data by over 2 standard deviations, while the `base` experiment fits the observations quite well. With the more recent meltrate observations from Shean et al. (2019), we are able to detect subtle features in meltrate patterns that the velocity independent parameterization misses in `constIO`. From these comparisons to the data, we determine the `constIO` experiment to be invalid.

The `smallVisc` experiment hints that the representation of subgrid-scale turbulence could explain reduced meltrates in velocity dependent simulations, and the `QGLeith` experiment makes this clear. The contrast between the equilibrium state of `QGLeith` and `Leith` further highlights the importance of employing flow aware, subgrid parameterizations for momentum *and* tracer transfer because of the thermodynamic interactions at the ice-ocean boundary. Enhanced diffusion directly underneath the ice shelf creates a layer of buoyant meltwater, which strengthens the horizontal density gradient. The inflow and outflow is subsequently invigorated by thermal wind, creating fast flowing "mini-gyres" underneath the ice shelf that are in close contact with the ice-ocean interface. Increased near-wall velocities then drive higher meltrates due to a velocity dependent ice-ocean parameterization. As a result, the `QGLeith` experiment exhibits some of its highest meltrates on either side of the ice plain in a zone bounded by the bathymetric ridge, similar to the satellite derived estimates from Shean et al. (2019).

Throughout the study we have focused our attention on simulating the cavity circulation and meltrate patterns under the Pine Island ice shelf. By focusing on developing a realistic numerical model of this particular ice shelf, we were able to validate our experiments with observational data. However, we expect that the thermal wind enhanced flow shown here would manifest in simulations of the cavity flow under other ice shelves in the Amundsen Sea. In particular, this mechanism relies simply on cyclonic flow inside of an enclosed cavity, where relatively warm and salty waters enter on the north/east boundary, and cold and fresh meltwater is driven outward on the south/west boundary, generated by an ice shelf above. Idealized experiments from Little et al. (2008) show that this general circulation is a common feature of ice shelves no matter the bathymetric or ice shelf slope orientation. Observations at the front of the Dotson (Jenkins et al., 2018) and Getz (Wåhlin et al., 2020) ice shelves indicate that such a cyclonic flow could exist under the shelves. Therefore, we surmise that a similar acceleration and meltrate enhancement would occur in other Amundsen Sea ice shelf cavity flow simulations, and suggest experimentation with flow aware subgrid-scale turbulence parameterizations in future studies.

For our application, we found the QG Leith parameterization formulated by Bachman et al. (2017) to provide a reasonable representation of subgrid processes. We note that this parameterization is based on QG turbulence, but this assumption may not be valid everywhere underneath the ice shelf. Determining the best representation of subgrid-scale ocean turbulence in this context, for instance with an even higher resolution nonhydrostatic model, could be considered for future work.

In all of the simulations shown, we made a number of assumptions that would need to be relaxed before using any of these models to simulate the time evolution of the ocean circulation under the Pine Island ice shelf, rather than a steady state solution as shown here. We did not simulate sea ice, which may be valid for the time period we wished to represent, January through March. However, sea ice is present in Pine Island Bay during other months of the year (Scambos et al., 1996). The atmospheric state is also not prescribed or simulated, since we assume that the data-informed open boundary conditions that force the model bear the imprint of atmospheric forcing. We additionally do not represent the effect of tides, based on previous results indicating that their inclusion has a relatively small effect on Pine Island ice shelf melting (Jourdain et al., 2019). Finally, our model omits the representation of ice shelf calving and iceberg melting within the computational domain. Representing these effects is not straightforward in ocean-only models, but is important future work for determining the ocean's role in and response to future changes in Pine Island Glacier mass loss (De Rydt et al., 2021).

Our computational models employed a high resolution grid: $\sim$600 m in the horizontal and 20 m in the vertical. Still, the simulated meltrate patterns show a "shadow region" near the grounding line that is essentially unresolved, but is an area of extremely high meltrates (> 100 m) in the satellite-derived estimates. This discrepancy suggests at least two areas of future work. First, the presence of subglacial discharge could be responsible for these high meltrates (Joughin et al., 2016). Specifically, subglacial discharge increases the buoyancy driven convection, and subsequently the meltrate, under the ice shelf at the source of the discharge near the grounding line (Jenkins, 2011). Discharge has been shown to be an important driver of melting under the Getz ice shelf (Wei et al., 2020). Additionally, very recent experiments have shown that subglacial discharge increases the meltrate in localized regions near the grounding line of the Pine Island ice shelf (Nakayama et al., 2021). It therefore seems necessary to incorporate this forcing mechanism into sub ice shelf cavity circulation models to further understand how discharge affects ice-ocean interactions and the relevant ocean dynamics. Secondly, representing meltrate patterns in these small-scale regions of ice shelves is even more computationally demanding for models that capture a larger spatial area, for instance in models of the entire Amundsen Sea Embayment. Our hope is that unstructured meshing strategies, (e.g. Timmermann et al., 2012; Kimura et al., 2013), can alleviate the computational burden for such simulations by resolving the fine-scale interactions underneath ice shelves, while using a larger grid-scale farther away from the cavity.

The numerical simulations shown here provide a view of the potential ocean dynamics underneath the Pine Island ice shelf. Our model validation process would not have been possible without in situ measurements of the ocean state and observations of ice topography, bathymetry, and meltrates from remote sensing data. Continuous observational coverage of this region, and of the marine margins of Antarctica in general, is essential to advance our understanding and verify our model-based predictions of ice-ocean interactions in the region.

Appendix A Data Processing

First we describe the steps we took to prepare the CTD and LADCP data for our study. We convert the vertical coordinate of the 2014 CTD and LADCP casts from pressure to depth using PyGSW (Campbell, 2012), assuming the mean latitude of the selected casts. For some of the casts, there is a discrepancy between the maximum depth of the data and the bathymetry regridded from BedMachine. In all instances, the data go deeper than our model's bathymetry, and we neglect these data values. There are no uncertainty estimates associated with potential temperature and salinity, so we use the values:

$$\sigma_{CTD,\theta} = 0.5\,^{\circ}\mathrm{C} \qquad \sigma_{CTD,S} = 0.05\,\mathrm{g/kg}\,.$$

We use these values to account for measurement error and, more importantly, representation error, accounting for spatiotemporally localized features that we cannot or do not want to infer during the optimal interpolation. The potential temperature data show spurious jumps, see for example in Figure 3(e) at $\sim$200 m depth. These temperature fluctuations are likely due to spatiotemporally localized phenomena that the optimal interpolation cannot succsefully capture, and we do not wish to represent in our equilibrium-state model. As such, we choose a fairly large uncertainty to cover these cases. The salinity data shows no such jumps, so it seems reasonable to provide a relatively small uncertainty. Finally, we note that we only use data with the highest quality control flag, but that this did not remove any data that we considered using.

Next, we describe the steps we took to prepare the mooring data for our study. We first bin average the temporal data to hourly time stamps. All data from a single instrument are assumed to be at a single depth level. This assumption ignores temporal depth variability, which we find to be reasonable because the amplitude of variability is well below the vertical resolution of our grid (20 m).

Some moorings do not have salinity data, so in these cases we represent salinity at these locations with data from the nearest CTD, which is <1 km away. In such instances, we double the observational uncertainty of the salinity estimate, noting that this makes it consistent with the CTD data described above: $\sigma_{CTD,S} = 2\sigma_{M,S}$. With in situ temperature and salinity at each mooring depth, we convert in situ temperature to potential temperature using PyGSW (Campbell, 2012).

In the case of the PIG_S mooring during 2014, data at some depth levels are inconsistent beyond one standard deviation from CTD casts taken at the same time period, less than 1 km away, as well as mooring data from BSR5 during 2009. These inconsistencies occur at 592, 525, 492, and 358 m depth, and in these cases the data from PIG_S is not considered, as it shows temperatures colder at depth than any other measurements available.

Acknowledgments

This study uses data from the Ice Sheeet Stability (iSTAR) and GEOTRACES projects, provided by the British Oceanographic Data Centre (BODC) and funded by NERC. The iStar8, PIG_N, and PIG_S mooring data together with the CTD data and 2014 LADCP data were collected from the BODC at `bodc.ac.uk`. The 2009 LADCP data and BSR5 mooring data were collected from the Marine Geoscience Data System, at `marine-geo.org` (Carbotte et al., 2007). The BedMachine dataset was gathered from (Morlighem, 2019). The satellite-based digital elevation model output was provided by David Shean. The model output and configuration files relevant to this study can be found at (Smith, 2021). I am grateful to Nora Loose, Martin Losch, and Patrick Heimbach for helpful comments that improved the manuscript. Financial support was provided in part by NASA MAP #80NSSC17K0558 and a JPL/Caltech Subcontract (ECCO Consortium).

References

Adcroft, A., Hill, C., & Marshall, J. (1997). Representation of topography by shaved cells in a height coordinate ocean model. *Monthly Weather Review*, *125*(9), 2293-2315. Retrieved from `https://doi.org/10.1175/1520-0493(1997)125<2293:ROTBSC>2.0.CO;2` doi: 10.1175/1520-0493(1997)125⟨2293:ROTBSC⟩2.0.CO;2

Adusumilli, S., Fricker, H. A., Medley, B., Padman, L., & Siegfried, M. R. (2020, August). Interannual variations in meltwater input to the Southern Ocean from Antarctic ice shelves. *Nature Geoscience*, 1–5. Retrieved 2020-08-11, from `http://www.nature.com/articles/s41561-020-0616-z` (Publisher: Nature Publishing Group) doi: 10.1038/s41561-020-0616-z

Arakawa, A., & Lamb, V. R. (1977, January). Computational Design of the Basic Dynamical Processes of the UCLA General Circulation Model. In J. Chang (Ed.), *Methods in Computational Physics: Advances in Research and Applica-*

tions (Vol. 17, pp. 173–265). Elsevier. Retrieved 2021-07-20, from https://www.sciencedirect.com/science/article/pii/B9780124608177500094 doi: 10.1016/B978-0-12-460817-7.50009-4

Årthun, M., Holland, P. R., Nicholls, K. W., & Feltham, D. L. (2013, September). Eddy-Driven Exchange between the Open Ocean and a Sub–Ice Shelf Cavity. *Journal of Physical Oceanography*, *43*(11), 2372–2387. Retrieved 2020-03-19, from https://journals.ametsoc.org/doi/10.1175/JPO-D-13-0137.1 (Publisher: American Meteorological Society) doi: 10.1175/JPO-D-13-0137.1

Assmann, K. M., Jenkins, A., Shoosmith, D. R., Walker, D. P., Jacobs, S. S., & Nicholls, K. W. (2013). Variability of Circumpolar Deep Water transport onto the Amundsen Sea Continental shelf through a shelf break trough. *Journal of Geophysical Research: Oceans*, *118*(12), 6603–6620. Retrieved 2020-04-14, from https://agupubs.onlinelibrary.wiley.com/doi/abs/10.1002/2013JC008871 (_eprint: https://agupubs.onlinelibrary.wiley.com/doi/pdf/10.1002/2013JC008871) doi: 10.1002/2013JC008871

Bachman, S. D., Fox-Kemper, B., & Pearson, B. (2017). A scale-aware subgrid model for quasi-geostrophic turbulence. *Journal of Geophysical Research: Oceans*, *122*(2), 1529–1554. Retrieved 2021-01-30, from https://agupubs.onlinelibrary.wiley.com/doi/abs/10.1002/2016JC012265 (_eprint: https://agupubs.onlinelibrary.wiley.com/doi/pdf/10.1002/2016JC012265) doi: https://doi.org/10.1002/2016JC012265

Campbell, L. (2012). *PyGSW: Python bindings for the TEOS-10 V3.0 GSW Oceanographic Toolbox in C.* Retrieved from https://github.com/lukecampbell/pygsw/

Campin, J.-M., Adcroft, A., Hill, C., & Marshall, J. (2004). Conservation of properties in a free-surface model. *Ocean Modelling*, *6*(3), 221 - 244. Retrieved from http://www.sciencedirect.com/science/article/pii/S146350030300009X doi: https://doi.org/10.1016/S1463-5003(03)00009-X

Campin, J.-M., Heimbach, P., Losch, M., Forget, G., edhill3, Adcroft, A., … dussin, r. (2021, June). *MITgcm/MITgcm: checkpoint67z.* Zenodo. Retrieved from https://doi.org/10.5281/zenodo.4968496 doi: 10.5281/zenodo.4968496

Carbotte, S. M., Ryan, W. B. F., O'Hara, S., Arko, R., Goodwillie, A., Melkonian, A., … Ferrini, V. L. (2007). *Antarctic Multibeam Bathymetry and Geophysical Data Synthesis: An On-Line Digital Data Resource for Marine Geoscience Research in the Southern Ocean* (U.S. Geological Survey Open-File Report No. 2007-1047). USGS. Retrieved from doi:10.3133/of2007-1047.srp002

Chelton, D. B., deSzoeke, R. A., Schlax, M. G., Naggar, K. E., & Siwertz, N. (1998, March). Geographical Variability of the First Baroclinic Rossby Radius of Deformation. *Journal of Physical Oceanography*, *28*(3), 433–460. Retrieved 2021-01-19, from https://journals.ametsoc.org/view/journals/phoc/28/3/1520-0485_1998_028_0433_gvotfb_2.0.co_2.xml (Publisher: American Meteorological Society Section: Journal of Physical Oceanography) doi: 10.1175/1520-0485(1998)028⟨0433:GVOTFB⟩2.0.CO;2

Christianson, K., Bushuk, M., Dutrieux, P., Parizek, B. R., Joughin, I. R., Alley, R. B., … Holland, D. M. (2016). Sensitivity of pine island glacier to observed ocean forcing. *Geophysical Research Letters*, *43*(20), 10,817–10,825. Retrieved from http://dx.doi.org/10.1002/2016GL070500 (2016GL070500) doi: 10.1002/2016GL070500

Corr, H. F. J., Doake, C. S. M., Jenkins, A., & Vaughan, D. G. (2001). Investigations of an "ice plain" in the mouth of Pine Island Glacier, Antarctica. *Journal of Glaciology*, *47*(156), 51–57. Retrieved 2021-08-11, from http://www.cambridge.org/core/journals/journal-of-glaciology/article/investigations-of-an-ice-plain-in-the-mouth-of-pine-island-glacier-antarctica/8F4FB58D150BC4892BBF81DFD8692B13 (Publisher:

Cambridge University Press) doi: 10.3189/172756501781832395

Dansereau, V., Heimbach, P., & Losch, M. (2014). Simulation of subice shelf melt rates in a general circulation model: Velocity-dependent transfer and the role of friction. *Journal of Geophysical Research: Oceans*, *119*(3), 1765–1790. Retrieved from https://agupubs.onlinelibrary.wiley.com/doi/abs/10.1002/2013JC008846 doi: 10.1002/2013JC008846

De Rydt, J., Holland, P. R., Dutrieux, P., & Jenkins, A. (2014). Geometric and oceanographic controls on melting beneath Pine Island Glacier. *Journal of Geophysical Research: Oceans*, *119*(4), 2420–2438. Retrieved 2019-06-25, from https://agupubs.onlinelibrary.wiley.com/doi/abs/10.1002/2013JC009513 doi: 10.1002/2013JC009513

De Rydt, J., Reese, R., Paolo, F. S., & Gudmundsson, G. H. (2021, January). Drivers of Pine Island Glacier speed-up between 1996 and 2016. *The Cryosphere*, *15*(1), 113–132. Retrieved 2021-01-12, from https://tc.copernicus.org/articles/15/113/2021/ (Publisher: Copernicus GmbH) doi: https://doi.org/10.5194/tc-15-113-2021

Dinniman, M., Asay-Davis, X., Galton-Fenzi, B., Holland, P., Jenkins, A., & Timmermann, R. (2016, December). Modeling Ice Shelf/Ocean Interaction in Antarctica: A Review. *Oceanography*, *29*(4), 144–153. Retrieved 2020-03-03, from https://tos.org/oceanography/article/modeling-ice-shelf-ocean-interaction-in-antarctica-a-review doi: 10.5670/oceanog.2016.106

Dotto, T. S., Naveira Garabato, A. C., Bacon, S., Holland, P. R., Kimura, S., Firing, Y. L., … Jenkins, A. (2019, September). Wind-Driven Processes Controlling Oceanic Heat Delivery to the Amundsen Sea, Antarctica. *Journal of Physical Oceanography*, *49*(11), 2829–2849. Retrieved 2020-04-14, from https://journals.ametsoc.org/doi/full/10.1175/JPO-D-19-0064.1 (Publisher: American Meteorological Society) doi: 10.1175/JPO-D-19-0064.1

Dupont, T. K., & Alley, R. B. (2005). Assessment of the importance of ice-shelf buttressing to ice-sheet flow. *Geophysical Research Letters*, *32*(4). Retrieved 2021-08-16, from https://agupubs.onlinelibrary.wiley.com/doi/abs/10.1029/2004GL022024 (_eprint: https://agupubs.onlinelibrary.wiley.com/doi/pdf/10.1029/2004GL022024) doi: 10.1029/2004GL022024

Dutrieux, P., De Rydt, J., Jenkins, A., Holland, P. R., Ha, H. K., Lee, S. H., … Schröder, M. (2014). Strong sensitivity of pine island ice-shelf melting to climatic variability. *Science*. Retrieved from http://science.sciencemag.org/content/early/2014/01/02/science.1244341 doi: 10.1126/science.1244341

Dutrieux, P., Vaughan, D. G., Corr, H. F. J., Jenkins, A., Holland, P. R., Joughin, I., & Fleming, A. H. (2013, September). Pine Island glacier ice shelf melt distributed at kilometre scales. *The Cryosphere*, *7*(5), 1543–1555. Retrieved 2020-05-02, from https://www.the-cryosphere.net/7/1543/2013/ (Publisher: Copernicus GmbH) doi: https://doi.org/10.5194/tc-7-1543-2013

Fox-Kemper, B., & Menemenlis, D. (2008). Can Large Eddy Simulation Techniques Improve Mesoscale Rich Ocean Models? *Ocean Modeling in an Eddying Regime*, 319–337. Retrieved 2021-02-02, from http://agupubs.onlinelibrary.wiley.com/doi/abs/10.1029/177GM19 (_eprint: https://onlinelibrary.wiley.com/doi/pdf/10.1029/177GM19) doi: 10.1029/177GM19

Fürst, J. J., Durand, G., Gillet-Chaulet, F., Tavard, L., Rankl, M., Braun, M., & Gagliardini, O. (2016, May). The safety band of Antarctic ice shelves. *Nature Climate Change*, *6*(5), 479–482. Retrieved 2021-07-20, from https://www.nature.com/articles/nclimate2912 (Bandiera_abtest: a Cg_type: Nature Research Journals Number: 5 Primary_atype: Research Publisher: Nature Publishing Group Subject_term: Climate and Earth system modelling;Cryospheric science Subject_term_id: climate-and-earth-system-modelling;cryospheric-science) doi: 10.1038/nclimate2912

Gent, P. R., & McWilliams, J. C. (1990, January). Isopycnal Mixing in Ocean Circulation Models. *Journal of Physical Oceanography*, *20*(1), 150–155. Retrieved 2021-07-20, from http://journals.ametsoc.org/view/journals/phoc/20/1/1520-0485_1990_020_0150_imiocm_2_0_co_2.xml (Publisher: American Meteorological Society Section: Journal of Physical Oceanography) doi: 10.1175/1520-0485(1990)020⟨0150:IMIOCM⟩2.0.CO;2

Goldberg, D. N., Gourmelen, N., Kimura, S., Millan, R., & Snow, K. (2019, January). How Accurately Should We Model Ice Shelf Melt Rates? *Geophysical Research Letters*, *0*(0). Retrieved 2019-01-18, from https://agupubs.onlinelibrary.wiley.com/doi/abs/10.1029/2018GL080383 doi: 10.1029/2018GL080383

Goldberg, D. N., Smith, T. A., Narayanan, S. H. K., Heimbach, P., & Morlighem, M. (2020). Bathymetric Influences on Antarctic Ice-Shelf Melt Rates. *Journal of Geophysical Research: Oceans*, *125*(11), e2020JC016370. Retrieved 2020-12-02, from http://agupubs.onlinelibrary.wiley.com/doi/abs/10.1029/2020JC016370 (_eprint: https://onlinelibrary.wiley.com/doi/pdf/10.1029/2020JC016370) doi: https://doi.org/10.1029/2020JC016370

Griffies, S. M. (1998, May). The Gent–McWilliams Skew Flux. *Journal of Physical Oceanography*, *28*(5), 831–841. Retrieved 2021-01-31, from http://journals.ametsoc.org/view/journals/phoc/28/5/1520-0485_1998_028_0831_tgmsf_2.0.co_2.xml (Publisher: American Meteorological Society Section: Journal of Physical Oceanography) doi: 10.1175/1520-0485(1998)028⟨0831:TGMSF⟩2.0.CO;2

Griffies, S. M., & Hallberg, R. W. (2000, August). Biharmonic Friction with a Smagorinsky-Like Viscosity for Use in Large-Scale Eddy-Permitting Ocean Models. *Monthly Weather Review*, *128*(8), 2935–2946. Retrieved 2021-01-17, from https://journals.ametsoc.org/view/journals/mwre/128/8/1520-0493_2000_128_2935_bfwasl_2.0.co_2.xml (Publisher: American Meteorological Society Section: Monthly Weather Review) doi: 10.1175/1520-0493(2000)128⟨2935:BFWASL⟩2.0.CO;2

Gudmundsson, G. H., Paolo, F. S., Adusumilli, S., & Fricker, H. A. (2019). Instantaneous Antarctic ice sheet mass loss driven by thinning ice shelves. *Geophysical Research Letters*, *46*(23), 13903–13909. Retrieved 2020-04-14, from https://agupubs.onlinelibrary.wiley.com/doi/abs/10.1029/2019GL085027 (_eprint: https://agupubs.onlinelibrary.wiley.com/doi/pdf/10.1029/2019GL085027) doi: 10.1029/2019GL085027

Hallberg, R. (2013, December). Using a resolution function to regulate parameterizations of oceanic mesoscale eddy effects. *Ocean Modelling*, *72*, 92–103. Retrieved 2019-10-11, from http://www.sciencedirect.com/science/article/pii/S1463500313001601 doi: 10.1016/j.ocemod.2013.08.007

Hattermann, T., Smedsrud, L. H., Nøst, O. A., Lilly, J. M., & Galton-Fenzi, B. K. (2014, October). Eddy-resolving simulations of the Fimbul Ice Shelf cavity circulation: Basal melting and exchange with open ocean. *Ocean Modelling*, *82*, 28–44. Retrieved 2021-07-19, from https://www.sciencedirect.com/science/article/pii/S1463500314000948 doi: 10.1016/j.ocemod.2014.07.004

Heimbach, P., & Losch, M. (2012). Adjoint sensitivities of sub-ice-shelf melt rates to ocean circulation under the pine island ice shelf, west antarctica. *Annals of Glaciology*, *53*(60), 59–69. doi: 10.3189/2012/AoG60A025

Hellmer, H., & Olbers, D. (1989). A two-dimensional model for the thermohaline circulation under an ice shelf. *Antarctic Science*, *1*(4), 325–336. doi: 10.1017/

S0954102089000490

Holland, D. M., & Jenkins, A. (1999). Modeling thermodynamic ice-ocean interactions at the base of an ice shelf. *Journal of Physical Oceanography*, *29*(8), 1787-1800. Retrieved from `https://doi.org/10.1175/1520-0485(1999)029<1787:MTIOIA>2.0.CO;2` doi: 10.1175/1520-0485(1999)029⟨1787:MTIOIA⟩2.0.CO;2

Jackett, D. R., & McDougall, T. J. (1995). Minimal adjustment of hydrographic profiles to achieve static stability. *Journal of Atmospheric and Oceanic Technology*, *12*(2), 381-389. Retrieved from `https://doi.org/10.1175/1520-0426(1995)012<0381:MAOHPT>2.0.CO;2` doi: 10.1175/1520-0426(1995)012⟨0381:MAOHPT⟩2.0.CO;2

Jacobs, S., & Huber, B. (2015). *Processed Temperature, Salinity, and Current Measurement Data from the Amundsen Sea acquired during the Nathaniel B. Palmer expedition NBP0901 (2009).* Interdisciplinary Earth Data Alliance (IEDA). Retrieved 2020-05-20, from `doi:10.1594/IEDA/322014` (Interdisciplinary Earth Data Alliance (IEDA). doi:10.1594/IEDA/322014. Accessed on 20 May 2020.)

Jacobs, S. S., Jenkins, A., Giulivi, C. F., & Dutrieux, P. (2011). Stronger ocean circulation and increased melting under pine island glacier ice shelf. *Nature Geoscience*, *4*(8), 519–523.

Jenkins, A. (2011, July). Convection-Driven Melting near the Grounding Lines of Ice Shelves and Tidewater Glaciers. *Journal of Physical Oceanography*, *41*(12), 2279–2294. Retrieved 2020-05-03, from `https://journals.ametsoc.org/doi/full/10.1175/JPO-D-11-03.1` (Publisher: American Meteorological Society) doi: 10.1175/JPO-D-11-03.1

Jenkins, A., Hellmer, H. H., & Holland, D. M. (2001). The role of meltwater advection in the formulation of conservative boundary conditions at an ice–ocean interface. *Journal of Physical Oceanography*, *31*(1), 285-296. Retrieved from `https://doi.org/10.1175/1520-0485(2001)031<0285:TROMAI>2.0.CO;2` doi: 10.1175/1520-0485(2001)031⟨0285:TROMAI⟩2.0.CO;2

Jenkins, A., Shoosmith, D., Dutrieux, P., Jacobs, S., Kim, T. W., Lee, S. H., ... Stammerjohn, S. (2018, October). West Antarctic Ice Sheet retreat in the Amundsen Sea driven by decadal oceanic variability. *Nature Geoscience*, *11*(10), 733–738. Retrieved 2020-04-26, from `http://www.nature.com/articles/s41561-018-0207-4` (Number: 10 Publisher: Nature Publishing Group) doi: 10.1038/s41561-018-0207-4

Joughin, I., Shean, D. E., Smith, B. E., & Dutrieux, P. (2016). Grounding line variability and subglacial lake drainage on Pine Island Glacier, Antarctica. *Geophysical Research Letters*, *43*(17), 9093–9102. Retrieved 2021-08-11, from `http://agupubs.onlinelibrary.wiley.com/doi/abs/10.1002/2016GL070259` (_eprint: https://onlinelibrary.wiley.com/doi/pdf/10.1002/2016GL070259) doi: 10.1002/2016GL070259

Jourdain, N. C., Molines, J.-M., Le Sommer, J., Mathiot, P., Chanut, J., de Lavergne, C., & Madec, G. (2019, January). Simulating or prescribing the influence of tides on the Amundsen Sea ice shelves. *Ocean Modelling*, *133*, 44–55. Retrieved 2020-06-16, from `http://www.sciencedirect.com/science/article/pii/S1463500318301203` doi: 10.1016/j.ocemod.2018.11.001

Kimura, S., Candy, A. S., Holland, P. R., Piggott, M. D., & Jenkins, A. (2013, July). Adaptation of an unstructured-mesh, finite-element ocean model to the simulation of ocean circulation beneath ice shelves. *Ocean Modelling*, *67*, 39–51. Retrieved 2021-08-02, from `https://www.sciencedirect.com/science/article/pii/S1463500313000449` doi: 10.1016/j.ocemod.2013.03.004

Kimura, S., Jenkins, A., Regan, H., Holland, P. R., Assmann, K. M., Whitt, D. B., ... Dutrieux, P. (2017). Oceanographic Controls on the Variability of Ice-Shelf Basal Melting and Circulation of Glacial Meltwater in the Amundsen Sea Embayment, Antarctica. *Journal of Geophysical Research: Oceans*, *122*(12), 10131–10155. Retrieved 2019-07-18, from `https://agupubs.onlinelibrary.wiley.com/doi/abs/10.1002/2017JC012926` doi: 10.1002/2017JC012926

Leith, C. (1996, November). Stochastic models of chaotic systems. *Physica D: Nonlinear Phenomena*, *98*(2-4), 481–491. Retrieved 2021-01-18, from `https://linkinghub.elsevier.com/retrieve/pii/0167278996001078` doi: 10.1016/0167-2789(96)00107-8

Leith, C. E. (1968, March). Diffusion Approximation for Two-Dimensional Turbulence. *The Physics of Fluids*, *11*(3), 671–672. Retrieved 2021-01-18, from `http://aip.scitation.org/doi/10.1063/1.1691968` (Publisher: American Institute of Physics) doi: 10.1063/1.1691968

Little, C. M., Gnanadesikan, A., & Hallberg, R. (2008, October). Large-Scale Oceanographic Constraints on the Distribution of Melting and Freezing under Ice Shelves. *Journal of Physical Oceanography*, *38*(10), 2242–2255. Retrieved 2021-08-11, from `http://journals.ametsoc.org/view/journals/phoc/38/10/2008jpo3928.1.xml` (Publisher: American Meteorological Society Section: Journal of Physical Oceanography) doi: 10.1175/2008JPO3928.1

Losch, M. (2008). Modeling ice shelf cavities in a z coordinate ocean general circulation model. *Journal of Geophysical Research: Oceans*, *113*(C8), n/a–n/a. Retrieved from `http://dx.doi.org/10.1029/2007JC004368` (C08043) doi: 10.1029/2007JC004368

Mack, S. L., Dinniman, M. S., Klinck, J. M., McGillicuddy, D. J., & Padman, L. (2019). Modeling Ocean Eddies on Antarctica's Cold Water Continental Shelves and Their Effects on Ice Shelf Basal Melting. *Journal of Geophysical Research: Oceans*, *124*(7), 5067–5084. Retrieved 2020-04-29, from `http://agupubs.onlinelibrary.wiley.com/doi/abs/10.1029/2018JC014688` (_eprint: https://onlinelibrary.wiley.com/doi/pdf/10.1029/2018JC014688) doi: 10.1029/2018JC014688

Marshall, J., Adcroft, A., Hill, C., Perelman, L., & Heisey, C. (1997). A finite-volume, incompressible navier stokes model for studies of the ocean on parallel computers. *Journal of Geophysical Research: Oceans*, *102*(C3), 5753–5766. Retrieved from `http://dx.doi.org/10.1029/96JC02775` doi: 10.1029/96JC02775

Martinson, D. G., & McKee, D. C. (2012, July). Transport of warm Upper Circumpolar Deep Water onto the western Antarctic Peninsula continental shelf. *Ocean Science*, *8*(4), 433–442. Retrieved 2021-08-02, from `https://os.copernicus.org/articles/8/433/2012/` (Publisher: Copernicus GmbH) doi: 10.5194/os-8-433-2012

Morlighem, M. (2019). *MEaSUREs BedMachine Antarctica, Version 1.* Boulder, Colorado USA. NASA National Snow and Ice Data Center Distributed Active Archive Center. Retrieved 2020-04-23, from `https://doi.org/10.5067/C2GFER6PTOS4` (Boulder, Colorado USA. NASA National Snow and Ice Data Center Distributed Active Archive Center. doi: https://doi.org/10.5067/C2GFER6PTOS4. Accessed on April 23, 2020.)

Morlighem, M., Rignot, E., Binder, T., Blankenship, D., Drews, R., Eagles, G., … Young, D. A. (2020, February). Deep glacial troughs and stabilizing ridges unveiled beneath the margins of the Antarctic ice sheet. *Nature Geoscience*, *13*(2), 132–137. Retrieved 2020-04-21, from `http://www.nature.com/articles/s41561-019-0510-8` (Number: 2 Publisher: Nature Publishing Group) doi: 10.1038/s41561-019-0510-8

Nakayama, Y., Cai, C., & Seroussi, H. (2021). Impact of Subglacial Freshwater Discharge on Pine Island Ice Shelf. *Geophysical Research Letters*, *48*(18), e2021GL093923. Retrieved 2021-10-18, from `http://`

onlinelibrary.wiley.com/doi/abs/10.1029/2021GL093923 (_eprint: https://agupubs.onlinelibrary.wiley.com/doi/pdf/10.1029/2021GL093923) doi: 10.1029/2021GL093923

Nakayama, Y., Manucharyan, G., Zhang, H., Dutrieux, P., Torres, H. S., Klein, P., ... Menemenlis, D. (2019, November). Pathways of ocean heat towards Pine Island and Thwaites grounding lines. *Scientific Reports*, *9*(1), 1–9. Retrieved 2019-11-27, from https://www.nature.com/articles/s41598-019-53190-6 doi: 10.1038/s41598-019-53190-6

Nakayama, Y., Menemenlis, D., Schodlok, M., & Rignot, E. (2017). Amundsen and bellingshausen seas simulation with optimized ocean, sea ice, and thermodynamic ice shelf model parameters. *Journal of Geophysical Research: Oceans*, *122*(8), 6180–6195. Retrieved from http://dx.doi.org/10.1002/2016JC012538 doi: 10.1002/2016JC012538

Nakayama, Y., Menemenlis, D., Zhang, H., Schodlok, M., & Rignot, E. (2018, August). Origin of Circumpolar Deep Water intruding onto the Amundsen and Bellingshausen Sea continental shelves. *Nature Communications*, *9*(1), 1–9. Retrieved 2020-04-14, from https://www.nature.com/articles/s41467-018-05813-1 (Number: 1 Publisher: Nature Publishing Group) doi: 10.1038/s41467-018-05813-1

Redi, M. H. (1982, October). Oceanic Isopycnal Mixing by Coordinate Rotation. *Journal of Physical Oceanography*, *12*(10), 1154–1158. Retrieved 2021-07-20, from http://journals.ametsoc.org/view/journals/phoc/12/10/1520-0485_1982_012_1154_oimbcr_2_0_co_2.xml (Publisher: American Meteorological Society Section: Journal of Physical Oceanography) doi: 10.1175/1520-0485(1982)012⟨1154:OIMBCR⟩2.0.CO;2

Scambos, T., Bohlander, J., & Raup, B. (1996). *Images of Antarctic Ice Shelves. January 2009 - April 2014.* Boulder, Colorado USA: National Snow and Ice Data Center. Retrieved from http://dx.doi.org/10.7265/N5NC5Z4N (Boulder, Colorado USA: National Snow and Ice Data Center. http://dx.doi.org/10.7265/N5NC5Z4N)

Schodlok, M. P., Menemenlis, D., Rignot, E., & Studinger, M. (2012). Sensitivity of the ice-shelf/ocean system to the sub-ice-shelf cavity shape measured by nasa icebridge in pine island glacier, west antarctica. *Annals of Glaciology*, *53*(60), 156-162. doi: 10.3189/2012AoG60A073

Shean, D. E., Joughin, I. R., Dutrieux, P., Smith, B. E., & Berthier, E. (2019, October). Ice shelf basal melt rates from a high-resolution digital elevation model (DEM) record for Pine Island Glacier, Antarctica. *The Cryosphere*, *13*(10), 2633–2656. Retrieved 2019-10-15, from https://www.the-cryosphere.net/13/2633/2019/ doi: https://doi.org/10.5194/tc-13-2633-2019

Smagorinsky, J. (1963, March). General Circulation Experiments with the Primitive Equations: I. The Basic Experiment. *Monthly Weather Review*, *91*(3), 99–164. Retrieved 2021-07-20, from https://journals.ametsoc.org/view/journals/mwre/91/3/1520-0493_1963_091_0099_gcewtp_2_3_co_2.xml (Publisher: American Meteorological Society Section: Monthly Weather Review) doi: 10.1175/1520-0493(1963)091⟨0099:GCEWTP⟩2.3.CO;2

Smith, T. (2021, Aug). *Model output for "Flow aware parameterizations invigorate the ocean circulation under the Pine Island ice shelf, West Antarctica".* figshare. Retrieved from https://doi.org/10.6084/m9.figshare.15455538.v1 doi: 10.6084/m9.figshare.15455538.v1

Stewart, A. L., & Thompson, A. F. (2015). Eddy-mediated transport of warm Circumpolar Deep Water across the Antarctic Shelf Break. *Geophysical Research Letters*, *42*(2), 432–440. Retrieved 2020-04-29, from http://agupubs.onlinelibrary.wiley.com/doi/abs/10.1002/2014GL062281 (_eprint: https://onlinelibrary.wiley.com/doi/pdf/10.1002/2014GL062281) doi: 10.1002/2014GL062281

St-Laurent, P., Klinck, J. M., & Dinniman, M. S. (2012, October). On the Role of Coastal Troughs in the Circulation of Warm Circumpolar Deep Water on Antarctic Shelves. *Journal of Physical Oceanography*, *43*(1), 51–64. Retrieved 2020-04-29, from http://journals.ametsoc.org/doi/10.1175/JPO-D-11-0237.1 (Publisher: American Meteorological Society) doi: 10.1175/JPO-D-11-0237.1

Thoma, M., Jenkins, A., Holland, D., & Jacobs, S. (2008). Modelling Circumpolar Deep Water intrusions on the Amundsen Sea continental shelf, Antarctica. *Geophysical Research Letters*, *35*(18). Retrieved 2021-07-20, from http://agupubs.onlinelibrary.wiley.com/doi/abs/10.1029/2008GL034939 (_eprint: https://onlinelibrary.wiley.com/doi/pdf/10.1029/2008GL034939) doi: 10.1029/2008GL034939

Thomas, R., Rignot, E., Kanagaratnam, P., Krabill, W., & Casassa, G. (2004). Force-perturbation analysis of Pine Island Glacier, Antarctica, suggests cause for recent acceleration. *Annals of Glaciology*, *39*, 133–138. Retrieved 2021-08-18, from http://www.cambridge.org/core/journals/annals-of-glaciology/article/forceperturbation-analysis-of-pine-island-glacier-antarctica-suggests-cause-for-recent-acceleration/C9C9146223E2D001F216A1228BD4D028 (Publisher: Cambridge University Press) doi: 10.3189/172756404781814429

Thurnherr, A. (2015). *Calibrated Hydrographic Data acquired with a LADCP from the Amundsen Sea acquired during the Nathaniel B. Palmer expedition NBP0901 (2009).* Integrated Earth Data Applications (IEDA). Retrieved 2020-05-20, from doi:10.1594/IEDA/322002 (Integrated Earth Data Applications (IEDA). doi:10.1594/IEDA/322002. Accessed on 20 May 2020.)

Thurnherr, A. M., Jacobs, S. S., Dutrieux, P., & Giulivi, C. F. (2014). Export and circulation of ice cavity water in Pine Island Bay, West Antarctica. *Journal of Geophysical Research: Oceans*, *119*(3), 1754–1764. Retrieved 2020-05-14, from https://agupubs.onlinelibrary.wiley.com/doi/abs/10.1002/2013JC009307 (_eprint: https://agupubs.onlinelibrary.wiley.com/doi/pdf/10.1002/2013JC009307) doi: 10.1002/2013JC009307

Timmermann, R., Wang, Q., & Hellmer, H. H. (2012). Ice-shelf basal melting in a global finite-element sea-ice/ice-shelf/ocean model. *Annals of Glaciology*, *53*(60), 303–314. Retrieved 2021-08-02, from https://www.cambridge.org/core/journals/annals-of-glaciology/article/iceshelf-basal-melting-in-a-global-finiteelement-seaiceiceshelfocean-model/B8724B766A10BD37FBB6B3F6C70F9089 (Publisher: Cambridge University Press) doi: 10.3189/2012AoG60A156

Webber, B. G. M., Heywood, K. J., Stevens, D. P., & Assmann, K. M. (2018, November). The Impact of Overturning and Horizontal Circulation in Pine Island Trough on Ice Shelf Melt in the Eastern Amundsen Sea. *Journal of Physical Oceanography*, *49*(1), 63–83. Retrieved 2020-05-16, from https://journals.ametsoc.org/doi/full/10.1175/JPO-D-17-0213.1 (Publisher: American Meteorological Society) doi: 10.1175/JPO-D-17-0213.1

Webber, B. G. M., Heywood, K. J., Stevens, D. P., Dutrieux, P., Abrahamsen, E. P., Jenkins, A., … Kim, T. W. (2017, April). Mechanisms driving variability in the ocean forcing of Pine Island Glacier. *Nature Communications*, *8*(1), 14507. Retrieved 2019-09-26, from http://www.nature.com/articles/ncomms14507 doi: 10.1038/ncomms14507

Wei, W., Blankenship, D. D., Greenbaum, J. S., Gourmelen, N., Dow, C. F., Richter, T. G., … Assmann, K. M. (2020, April). Getz Ice Shelf melt enhanced by freshwater discharge from beneath the West Antarctic Ice Sheet. *The Cryosphere*, *14*(4), 1399–1408. Retrieved 2021-10-18, from https://tc.copernicus.org/articles/14/1399/2020/ doi: 10.5194/

tc-14-1399-2020

Wåhlin, A. K., Steiger, N., Darelius, E., Assmann, K. M., Glessmer, M. S., Ha, H. K., … Viboud, S. (2020, February). Ice front blocking of ocean heat transport to an Antarctic ice shelf. *Nature*, *578*(7796), 568–571. Retrieved 2020-02-28, from http://www.nature.com/articles/s41586-020-2014-5 (Number: 7796 Publisher: Nature Publishing Group) doi: 10.1038/s41586-020-2014-5

Zhuang, J., Dussin, R., Jüling, A., & Rasp, S. (2020, March). *JiaweiZhuang/xESMF: v0.3.0 Adding ESMF.LocStream capabilities.* Zenodo. Retrieved from https://doi.org/10.5281/zenodo.3700105 doi: 10.5281/zenodo.3700105

Supporting Information for "Flow aware parameterizations invigorate the ocean circulation under the Pine Island ice shelf, West Antarctica"

Timothy A. Smith[1,2,3]

[1]Oden Institute for Computational Engineering and Sciences, The University of Texas at Austin, Austin, Texas

[2]Cooperative Institute for Research in Environmental Sciences (CIRES) at the University of Colorado Boulder

[3]National Oceanic and Atmospheric Administration (NOAA) Physical Sciences Laboratory (PSL)

Contents of this file

Text S1. Optimal interpolation methodology

The prescribed ocean state at the western boundary of the computaional domain serves as an important forcing mechanism for the ice shelf and ocean circulation. Our goal is to determine the most realistic values for the temperature, salinity, and normal velocity fields at the boundary, given the available CTD and LADCP observations during 2009 and 2014. To do this in a relatively straightforward fashion, we find the solution to the optimal interpolation (OI) problem for the generic parameter field $\mathbf{m} \coloneqq [\boldsymbol{\theta}_W^T, \mathbf{S}_W^T, \mathbf{u}_W^T]^T \in \mathbb{R}^{N_m}$:

$$\mathbf{m}_{OI} = \underset{\mathbf{m}\in\mathbb{R}^{N_m}}{\arg\min}\, \mathcal{J}(\mathbf{m}) \tag{1}$$

where

$$\mathcal{J}(\mathbf{m}) = \frac{1}{2}||f(\mathbf{m}) - \mathbf{d}||^2_{\Gamma^{-1}_{\text{Obs}}} + \frac{1}{2}||\mathbf{m} - \mathbf{m}_0||^2_{\Gamma^{-1}_{\text{prior}}} .$$

Here $f : \mathbb{R}^{N_m} \ni \mathbf{m} \to \mathbf{d} \in \mathbb{R}^{N_d}$ is simply a linear interpolation operator, mapping the parameter fields to the location of available data.

As a matter of computational convenience we make the following assumptions. First, we assume that each parameter field is independent from one another, allowing us to solve three OI problems for temperature, salinity, and velocity separately. Second, we assume that the observational and prior uncertainties can be described by Gaussian statistics. We further assume that the observations are independent, such that $\Gamma_{\text{Obs}} = \text{diag}\{\sigma_i^2\}_{i=1}^{N_\mathbf{d}}$. Observational uncertainties (standard deviations) are assumed to be 0.5°C for potential temperature and 0.05 g/kg for salinity as they are not provided, see Appendix A in the main text for details. The LADCP velocity data is provided with uncertainty estimates, which we use.

We specify the prior covariance as Matérn class due to the link between Matérn class Gaussian fields and the solution of the elliptic stochastic partial differential equation

(Lindgren et al., 2011):

$$\Big(\delta(\mathbf{x}) - \nabla \cdot K(\mathbf{x})\nabla\Big)m(\mathbf{x}) = \mathcal{W}(\mathbf{x}) \qquad \mathbf{x} \in \partial\Omega_{OBW}\,, \tag{2}$$

where $\mathcal{W}(\mathbf{x})$ is a standard white noise process. We employ the empirical relationship provided in Lindgren et al. (2011) and choose $\delta(\mathbf{x})$ and $K(\mathbf{x})$ such that the parameter fields exhibit a correlation of 0.1 at separation lengths: 18 km meridionally and 150 m vertically.

The last ingredient is the initial guess for the OI problem, $\mathbf{m}_0$. Simple inspection of the temperature and salinity data shows that these fields have mostly vertical structure, with slight variations in the depth of thermocline and halocline due to their horizontal location. Therefore, we specify $\boldsymbol{\theta}_0$ and $\mathbf{S}_0$ as vertical profiles based on polynomial regressions of the data. We note that using this has similar results to specifying $\boldsymbol{\theta}_0 = 0$°C and $\mathbf{S}_0 =$ 34.36 g/kg, but the former provides a better fit to the observations. The spatial structure of the velocity data is less obvious *a priori* and we therefore specify $\mathbf{u}_0 = 0$ m/s.

Given these assumptions and specifications, the minimization problem in equation (1) is linear and we can write the solution to each independent OI problem as:

$$\boldsymbol{\theta}_{OI} = \boldsymbol{\theta}_0 + \Gamma_{\text{post}} F^T \Gamma_{\text{Obs}}^{-1}\Big(\mathbf{d} - F\boldsymbol{\theta}_0\Big)$$
$$\Gamma_{\text{post}} = \left(F^T \Gamma_{\text{Obs}}^{-1} F + \Gamma_{\text{prior}}^{-1}\right)^{-1} .$$

Here, potential temperature is shown as an example, and a similar solution is obtained for salinity and velocity. Before these results can be used directly as forcing for the ocean model, the spatial integral is removed from the zonal velocity:

$$u_W(\mathbf{x}) = u_{OI} - \int_{\partial\Omega_{\text{open}}} u_{OI}\, d\mathbf{x}\,.$$

Removing the spatial mean ensures that we do not add or remove mass from the domain, and there is no artificial sea level rise during the spinup to reach equilibrium. In practice, this corresponds to removing a small average velocity: 0.00943 m/s. The resulting fields are shown in comparison to the observational data in Figure S1.

References

Lindgren, F., Rue, H., & Lindström, J. (2011). An explicit link between gaussian fields and gaussian markov random fields: the stochastic partial differential equation approach. *Journal of the Royal Statistical Society: Series B (Statistical Methodology)*, *73*(4), 423–498. Retrieved from http://dx.doi.org/10.1111/j.1467-9868.2011.00777.x doi: 10.1111/j.1467-9868.2011.00777.x

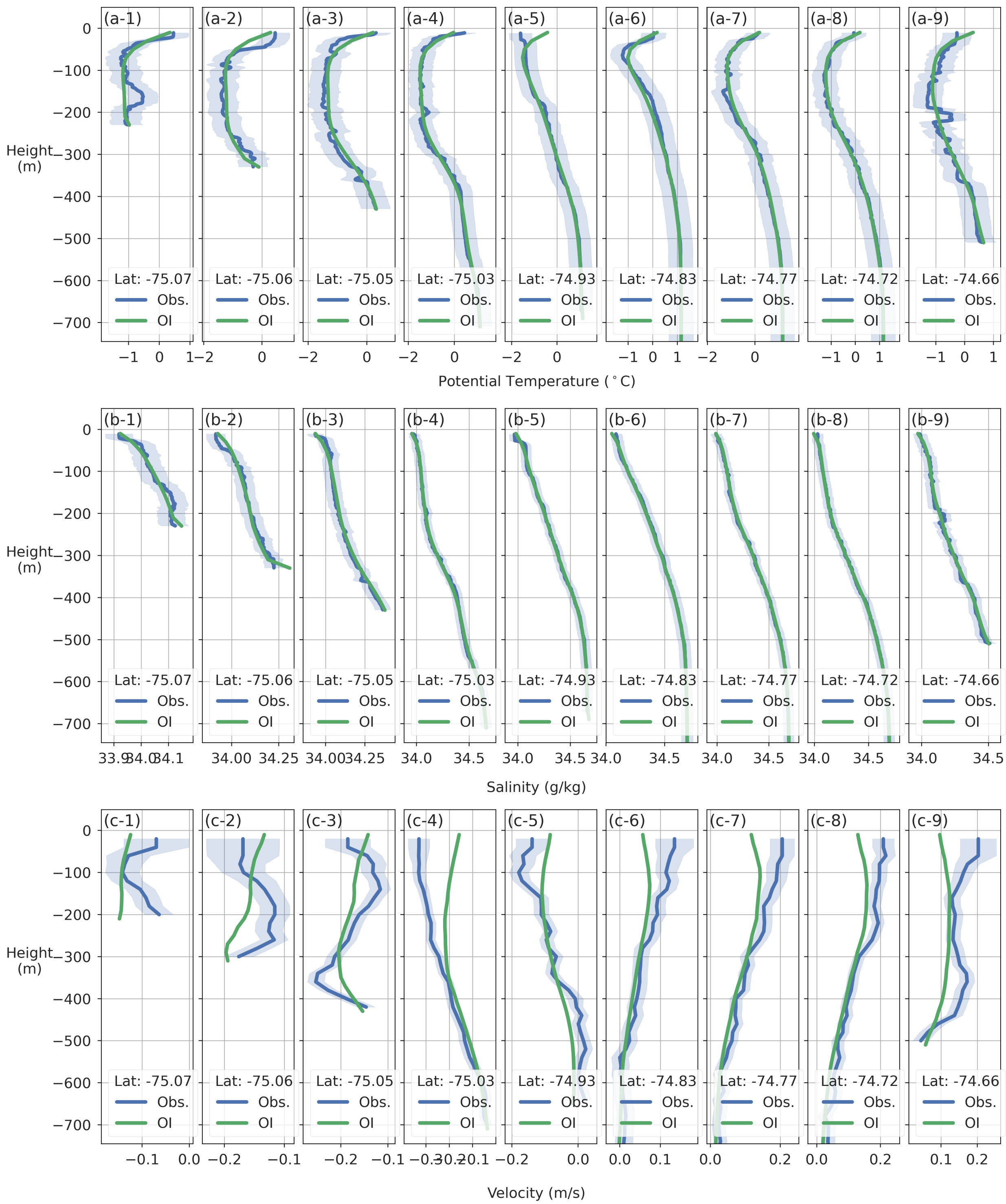

Figure S1. Optimal interpolation results (OI; green line) compared to data (Obs; blue line) at all CTD/LADCP locations used to compute open the open boundary conditions. (a-1 – a-9) potential temperature, (b-1 – b-9) salinity, (c-1 – c-9) zonal velocity.